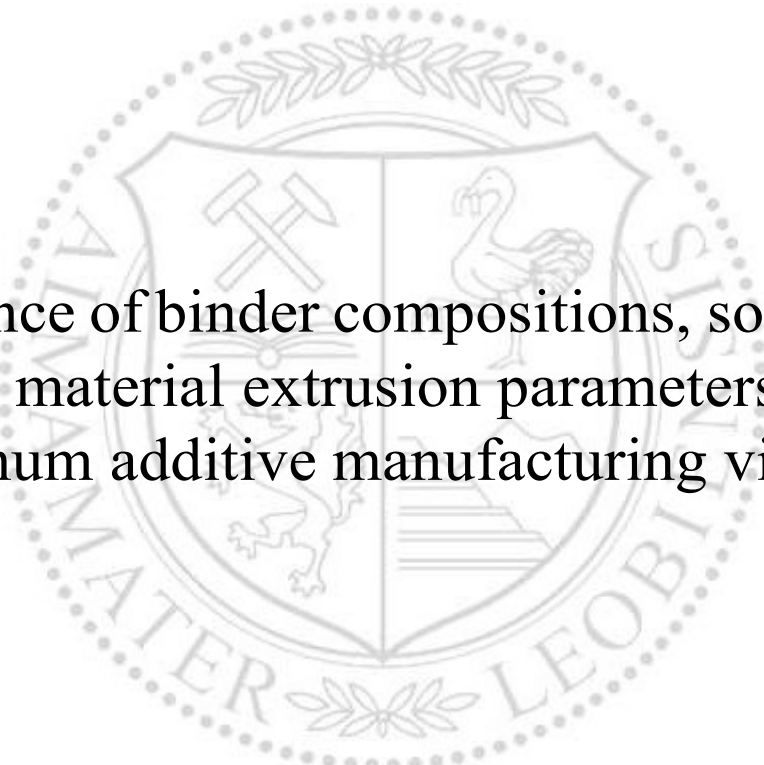




Chair of Polymer Processing

Master's Thesis



Influence of binder compositions, solvents,
and material extrusion parameters on
aluminum additive manufacturing via SDS

Margarete Hufnagl, BSc

June 2024



EIDESSTÄTTLICHE ERKLÄRUNG

Ich erkläre an Eides statt, dass ich diese Arbeit selbstständig verfasst, andere als die angegebenen Quellen und Hilfsmittel nicht benutzt, den Einsatz von generativen Methoden und Modellen der künstlichen Intelligenz vollständig und wahrheitsgetreu ausgewiesen habe, und mich auch sonst keiner unerlaubten Hilfsmittel bedient habe.

Ich erkläre, dass ich den Satzungsteil „Gute wissenschaftliche Praxis“ der Montanuniversität Leoben gelesen, verstanden und befolgt habe.

Weiters erkläre ich, dass die elektronische und gedruckte Version der eingereichten wissenschaftlichen Abschlussarbeit formal und inhaltlich identisch sind.

Datum 14.05.2024

Unterschrift Verfasser/in
Margarete Hufnagl

Acknowledgment

This master's thesis was conducted as part of the ALF³ project, and I am immensely grateful to Univ.-Prof. Dipl.-Ing. Dr. mont. Clemens Holzer for enabling this research.

I extend my special thanks to M.Sc. Vahid Momeni and Dipl.-Ing. Stephan Schuschnigg for their invaluable guidance and professional support throughout my practical work.

Additionally, I would like to express my appreciation to all the members of the department for their excellent cooperation and substantial support.

Abstract

Material extrusion (MEX) is an additive manufacturing technique that can serve as the shaping step to create green parts, in the shape, debinding, and sintering (SDS) process of metal specimens. Employing SDS with MEX for aluminum offers a promising cost-effective production method for parts with complex geometry. However, this process requires a highly filled thermoplastic binder system for AlSi1 powder, to produce filament for the MEX process. The filament is needed to feed the 3D printer with the material required to shape the specimens.

An important challenge in utilizing MEX in SDS is the development of an appropriate binder composition that meets the requirements for the printing step as well as the debinding and sintering step. For the printing step, the filaments should be a combination of the following characteristics - tough, flexible and low viscous. The debinding step requires a dual-component binder system, where one component is soluble in the chosen solvent, while the other one is resistant to this solvent. The solvents evaluated in this master thesis are cyclohexane, acetone, and water. Additionally, the binder components should possess a lower thermal degradation temperature than the sintering temperature of aluminium. This is particularly challenging since the AlSi1 sintering temperature is similar to the degradation temperature of most thermoplasts. This is important because the binder must be completely removed to reduce the risk of high levels of residual oxygen and carbon, as well as the formation of Al_2O_3 , which can significantly affect the quality of the sintered part.

The objective of the master thesis, conducted as part of the project ALF³, was to enhance the understanding of the binder components required for this specific process.

Therefore the impact of various backbone materials as a binder component, along with the influence of several main binder materials on the rheological, thermal, printing, and debinding properties of the AlSi1 feedstocks were analyzed. The thermal properties of the binder systems and feedstocks were investigated using differential scanning calorimetry (DSC) and thermogravimetric analysis (TGA) testing. The rheological behavior was examined using high-pressure capillary rheometers. Additionally, the contact angle measurements were performed to see the effect on the wetting behavior of the binder components and the particle distribution of AlSi1 in the Feedstock. This was followed by the production of feedstock filaments, analysis with scanning electron microscopy (SEM) and MEX printing.

The findings demonstrated the possibility of producing three optimized binder formulations for each solvent employed in the debinding process. Moreover, there is potential to refine the printing process to meet the specific demands of highly packed filaments with a volume fraction of 55 vol.%.

Kurzfassung

Materialextrusion (MEX) ist eine additive Fertigungstechnik, die als Formgebungsschritt zur Herstellung von Grünteilen im SDS-Prozess (Shape, Debinding and Sintering) von Metall dienen kann. Der Einsatz von SDS mit MEX für Aluminium bietet eine vielversprechende, kostengünstige Produktionsmethode für Teile mit komplexer Geometrie. Dieses Verfahren erfordert jedoch ein hochgefülltes thermoplastisches Bindersystem Feedstock für AlSi1-Pulver zur Herstellung von Filamenten für das MEX-Verfahren. Das Filament wird benötigt, um den 3D-Drucker mit dem Material zu versorgen, das für die Formgebung der Probekörper erforderlich ist.

Eine wichtige Herausforderung bei der Anwendung von MEX in SDS ist die Entwicklung einer geeigneten Binder-Zusammensetzung, die den Anforderungen sowohl für den Druckschritt als auch für den Entbinderungs- und Sinterungsschritt gerecht wird. Für den Druckschritt sollten die Filamente eine Kombination der folgenden Eigenschaften aufweisen: fest, flexibel und niedrig viskos. Für den Entbinderungsprozess wird ein Zweikomponenten-Bindersystem benötigt, bei dem eine Komponente in dem gewählten Lösungsmittel löslich ist, während die andere Komponente gegen dieses Lösungsmittel beständig ist. Die in dieser Masterarbeit untersuchten Lösungsmittel waren Cyclohexan, Aceton und Wasser. Außerdem sollten die Binderkomponenten eine niedrigere thermische Zersetzungstemperatur aufweisen als die Sintertemperatur von Aluminium. Dies ist eine besondere Herausforderung, da die Sintertemperatur von AlSi1 ähnlich hoch ist wie die Zersetzungstemperatur von den meisten Thermoplasten. Dies ist wichtig, da der Binder vollständig entfernt werden muss, um das Risiko eines hohen Restsauerstoff- und -kohlenstoffgehalts sowie der Bildung von Al_2O_3 zu verringern, was die Qualität des gesinterten Teils erheblich beeinträchtigen kann.

Ziel der Masterarbeit, die im Rahmen des Projekts ALF³ durchgeführt wurde, war es, das Verständnis der für diesen speziellen Prozess erforderlichen Binderkomponenten zu verbessern.

Daher wurden die Auswirkungen verschiedener Backbone-Materialien als Binderkomponente sowie der Einfluss verschiedener löslicher Binderkomponenten auf die rheologischen, thermischen, drucktechnischen und Entbinderungeigenschaften von AlSi1-Feedstock analysiert. Die thermischen Eigenschaften von Bindemittelsystemen und Feedstock wurden mit Hilfe der Differential-Scanning-Kalorimetrie (DSC) und der thermogravimetrischen Analyse (TGA) untersucht. Das rheologische Verhalten wurde mit Hochdruck-Kapillarrheometern untersucht. Zusätzlich wurden Kontaktwinkelmessungen durchgeführt, um den Einfluss auf das Benetzungsverhalten der Binderkomponenten und die Partikelverteilung von AlSi1 im Feedstock zu ermitteln. Es folgten die Herstellung von Feedstock-Filamenten, die Untersuchungen mit Rasterelektronenmikroskopie (SEM) und der MEX-Druck.

Die Ergebnisse zeigten, dass es möglich ist, drei optimierte Binderformulierungen für jedes im Entbinderungsprozess verwendete Lösungsmittel herzustellen. Darüber hinaus konnte der Druckprozess optimiert werden, so dass er den spezifischen Anforderungen von hochgefüllten, 55 vol.% AlSi1, Filamenten mit gerecht wird.

Table of contents

1	INTRODUCTION AND OBJECTIVES	7
1.1	STARTING POSITION	7
1.2	GOAL	7
2	STATE OF THE ART	9
2.1	ADDITIVE MANUFACTURING.....	9
2.1.1	Steps in the AM Process	9
2.1.1.1	Classification of AM Technology	10
2.1.1.2	Direct Energy Deposition	10
2.1.1.3	Powder Bed Fusion	10
2.1.1.4	Binder Jetting	10
2.1.1.5	Material Jetting.....	11
2.1.1.6	Vat Photopolymerisation	11
2.1.1.7	Material Extrusion	11
2.2	METAL MATERIAL EXTRUSION	12
2.2.1	Feedstock Preparation - Compounding of a Multimaterial	12
2.2.2	Filament Making	13
2.2.3	Shaping - Printing	14
2.2.4	Debinding	14
2.2.5	Sintering	15
3	HYPOTHESES AND APPROACH	17
3.1	HYPOTHESES.....	17
3.1.1	Cyclohexane Debinding Binder System	17
3.1.2	Acetone Debinding Binder System.....	17
3.1.3	Water Debinding Binder System.....	17
3.2	APPROACH.....	18
4	MATERIALS AND METHODS	20
4.1	MATERIALS	20
4.2	PREPARATION OF COMPOUNDS.....	23
4.3	HIGH-PRESSURE CAPILLARY RHEOMETER RHEOGRAPH 2002 GÖTTFERT	24
4.4	DEBINDING.....	25
4.5	DSC.....	25
4.6	TGA.....	26
4.7	CONTACT ANGLE MEASUREMENTS	26
4.8	PRINTING.....	28
4.9	MORPHOLOGY ANALYSES	28
5	RESULTS AND DISCUSSION	29
5.1	EVALUATION OF THE TORQUE MEASUREMENTS	29
5.2	EVALUATION OF THE VISCOSITY	33
5.3	EVALUATION OF THE THERMOGRAVIMETRIC ANALYSIS	38
5.4	EVALUATION OF THE DSC RESULTS	47
5.5	EVALUATION OF THE PRINTING RESULTS.....	57
5.6	EVALUATION OF THE DEBINDING RESULTS	61
5.6.1	Acetone based Debinding	61
5.6.2	Cyclohexane based Debinding.....	64

5.6.3	Water based Debinding	65
5.7	EVALUATION OF THE CONTACT ANGLE.....	66
5.8	EVALUATION OF THE MORPHOLOGICAL MEASUREMENTS	67
6	CONCLUSION	70
7	LITERATURE.....	72
8	LIST OF FIGURES	74
9	LIST OF TABLES.....	77
10	ABBREVIATIONS AND SYMBOLS.....	78
11	APPENDIX	80

1 Introduction and Objectives

1.1 Starting Position

The master's thesis was completed as part of the ALF³ project. The project ALF³ focuses on additive manufacturing (AM) with aluminum, which is a crucial material for lightweight design in several industries. The drawbacks of current technologies like powder bed fusion of Aluminum with a Laser beam (PBF-LB/Al) (high cost, handling of powder) may be overcome by employing filament printing. Additional benefits of filament printing include the ability to blend multiple materials in one part or create closed chambers inside pieces. The mechanical performance and quality of additive manufacturing components are improved by employing different materials, and the process productivity is increased. The possibilities made available by the use of filament printing can further improve the functioning of AM aluminum parts.

1.2 Goal

The aim of this work was the development of binder systems for aluminum additive manufacturing. The manufacturing method consists of feedstock preparation, shaping with an additive Material Extrusion (MEX) printer, debinding, and sintering. Metal material extrusion (Metal MEX) is very similar to conventional metal injection molding (MIM). These processes are both considered as Shaping, Debinding, and Sintering (SDS) process techniques. Due to the same process steps as in the MIM production of metal parts, the development of binder systems for metal MEX can be in general based on the experience gained in the development of MIM binder systems [28].

The printed part is referred to as "Green Part," the debinded part as "Brown Part," and sometimes the sintered metal part as "White Part". In the first step, green parts are printed from a metal/polymer composite filament, during which polymer is melted as a binder but metal particles remain solid. Subsequently, brown parts are obtained by debinding the green parts to remove the majority of the polymeric binder. The remaining polymer binder in the brown portions prevents the metal particulates from separating, thereby preserving the shape of the brown parts. Finally, in the sintering step, they degrade and sintering fuses the metal particles into a dense solid [8, 13].

Several factors, including high powder loading, homogeneous powder-binder distribution, adequate filament stiffness, low viscosity during printing, and absence of binder residue before final sintering, must be taken into account when designing metal-binder feedstock for use in metal MEX. A large powder loading (> 55 vol.%) is often anticipated to minimize shrinkage and shape distortion during sintering. On the other side, a very high powder loading may impede feedstock flow through the printing nozzle, causing uneven printing. Similarly to this, a non-uniform powder dispersion in the polymer matrix might cause processing issues, because of the high viscosity variations and related pressure changes in the nozzle, which can result in inconsistent printing. To prevent filament breaking, adequate filament strength and stiffness are required. Additionally, the viscosity of the material, which is influenced by composition and the ratio of powder to binder as well as temperature and shear rate, directly affects the printing process [3, 27, 32].

The final attributes may be significantly influenced by the characteristics of the feedstock components. One of the most important feedstock elements that must be optimized for each powder is the backbone, particularly for Aluminum because processing this oxygen-sensitive metal is rather difficult. Aluminum's sintering temperature (550 °C) is close to the temperature at which most polymers degrade. Before sintering, the binder must be completely removed during debinding, otherwise, the finished product may develop certain mechanical flaws due to the existence of large voids and associated flaws that cannot be eliminated during sintering. Also, high levels of residual oxygen and carbon reduce the mechanical performance of the Al alloys, which is another issue with partial debinding. Additionally, the presence of Al₂O₃, which is very stable, will affect the sintering process. Al₂O₃ cannot be reduced during sintering [25, 29].

Due to the very different process steps, it is important to develop a binder system that works for each step. For this reason, the different binder-aluminum systems were tested for their thermal, and rheological properties, printability, debinding properties, and sintering quality.

In this master thesis the following compositions of binder systems, see Table 1, were tested and analyzed for the above-mentioned properties.

Table 1 Overview of chosen binder systems

	BACKBONE	MAIN BINDER	POWDER	SOLVENT
TYPE 1	PLA	TPE 1	AlSi1	Cyclohexane
TYPE 2	PP			
TYPE 3	HDPE			
TYPE 4	TSEB/ TPE 3/ TPC	ASA		Acetone
TYPE 5	HDPE	TPE 4 (20 A /40 A /70 A)		
TYPE 6	PP			
TYPE 7	PLA	PVA		Water
TYPE 8	TSEB			
TYPE 9	ASA			

The individual binder systems were additionally compared for different volume fractions. The best formulation of each type was then selected and further optimization was attempted.

2 State of the art

2.1 Additive Manufacturing

Additive manufacturing, commonly known as 3D printing, is successfully used as prototyping in many industries, such as automotive, aerospace, and medical. This offers the possibility to produce geometrically complex components, where materials are applied layer by layer according to a computer-aided design model.

According to the International Standard EN ISO/ASTM 52900:2021(en), additive manufacturing is the *"process that produces components from 3D model data by joining material, typically layer by layer, as opposed to subtractive and forming manufacturing methods."* Compared to other manufacturing technologies, additive manufacturing offers several key advantages. There is a significant reduction in material consumption compared to the subtractive manufacturing process. Processing equipment such as tools and molds are not needed, which provides greater flexibility. More complex geometries are possible and costs for small series can be saved. A disadvantage of additive manufacturing can be the limited build space, slow processing times, as well as the need for post-processing of the surface to improve the surface finish [1, 9].

Advances in digital and equipment technology are making the use of additive manufacturing in small-batch production more economically attractive. AM can overcome the limitations of traditional manufacturing processes, opening up new constructive freedom in part design.

2.1.1 Steps in the AM Process

The Additive Manufacturing (AM) process starts, see Fig. 1, with a flawless 3D data set that contains all the necessary geometric information for the part to be produced, commonly known as the virtual product model. This data set, which can be acquired through different methods like 3D CAD programs or scanning, needs to portray a closed 3D volume and could also incorporate supports created by a separate program if needed for the AM process. The AM front end is responsible for initiating the AM process. The STL format is widely used for transmitting 3D data to AM machines, along with other formats such as Additive Manufacturing File (AMF), Virtual Reality Modeling Language (VRML), and Polygon File Format (PLY) [9, 10].

After data set modeling, a suitable AM material and process are chosen, with process parameters usually obtained from manufacturers' databases or determined through tests. Typically, the software, which enables communication between the operator and the machine, is integrated to the machine but can also be offered by a third party. Before the building process begins, components are placed and specific settings are configured for the machine, resulting in a layer-by-layer automated assembly until the part is finished. Post-processing steps typically involve cooling, solvent cleaning, support removal, and other treatments such as sintering or varnishing. These steps help differentiate between the initial additive manufacturing steps and the subsequent finishing processes [9, 10].

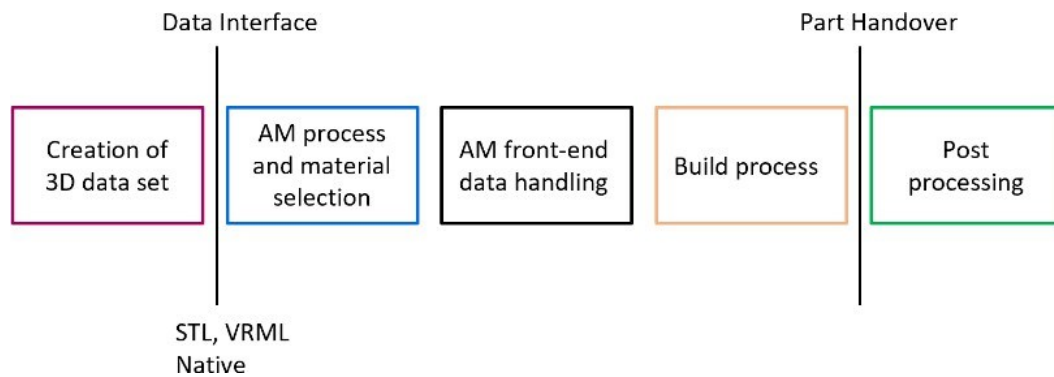


Fig. 1 Process chain of additive manufacturing [10]

2.1.1.1 Classification of AM Technology

Additive manufacturing can be classified into different sub-areas. Each of these sub-areas has its own fundamentals and materials. The suitability of a process depends on the material used and the desired component properties.

In AM of metals, several methods are available, such as direct energy deposition (DED), powder bed fusion (PBF), binder jetting (BJT), material jetting (MJT), VAT Photopolymerization (VPP) and material extrusion (MEX).

2.1.1.2 Direct Energy Deposition

DED is a collection of additive manufacturing technologies that involve the simultaneous addition of material along with heat input. The heat input can be generated using a laser, electron beam, or plasma arc. The material used for feeding is either in the form of metal powder or wire. Powders yield reduced deposition efficiency compared to metal wires because only a portion of the total powder is melted and attached to the substrate [26].

2.1.1.3 Powder Bed Fusion

In a thin layer, the material to be processed is applied in powder form to a powder bed and selectively sintered or melted with the aid of laser radiation or electron beam, and it forms a solid material layer after solidification. This process is repeated layer by layer, by lowering the powder bed and applying a new thin layer until the entire product contour has been created. Metals, plastics, and ceramics can be used as materials [9].

2.1.1.4 Binder Jetting

Similar to powder bed-based fusion, a powder bed is present, which is selectively bonded by a liquid binder. After the completion of a layer, the powder bed is moved down and a new layer of powder is applied. The binder can also be colored and the print heads are similar to inkjet printers and can also produce multicolored components. To improve strength, the components can still be infiltrated after completion. Plastic, inorganic powders, plaster, ceramics, or metal can be used as powder material, whereby the metals are usually sintered after production [9].

2.1.1.5 Material Jetting

In material jetting, a photopolymer is ejected from a printhead to create a part layer by layer. When the droplets are deposited on the build platform, they are directly cured and solidified with UV light. The material jetting process requires a support structure that is often 3D printed simultaneously during build from a soluble material. The support material is then removed during post-processing [9].

2.1.1.6 Vat Photopolymerisation

The solidification of liquid monomers works on the principle of photopolymerization. Viscous, non-crosslinked or low-crosslinked monomers containing photo-initiators are used for this purpose. Upon irradiation with a UV light source, polymerization starts, causing the liquid polymer to react to form a solid polymer [9, 11].

In the Vat photopolymerization (VPP) radiation such as ultraviolet (UV) and visible light triggers the selective polymerization of the liquid-photosensitive resin. This light-curing resin is partially cured, forming a durometer. After one layer is cured, the carrier plate is lowered and the top layer is wetted again with the resin. This manufacturing process continues from the bottom up until the 3D component is complete. The finished components are polymerized to about 95 % in the system and then post-cured and cleaned outside the machine. Acrylic resins, epoxy resins and vinyl ether resins can be used in this process [6, 9].

2.1.1.7 Material Extrusion

MEX, also known as Fused Deposition Modeling (FDM™) is an additive manufacturing process in which polymers or polymer-based compounds are processed as filaments or granules. There are various classifications for MEX, based on the type of extruder used, like plunger, filaments, or screw, which handle the materials in various ways.

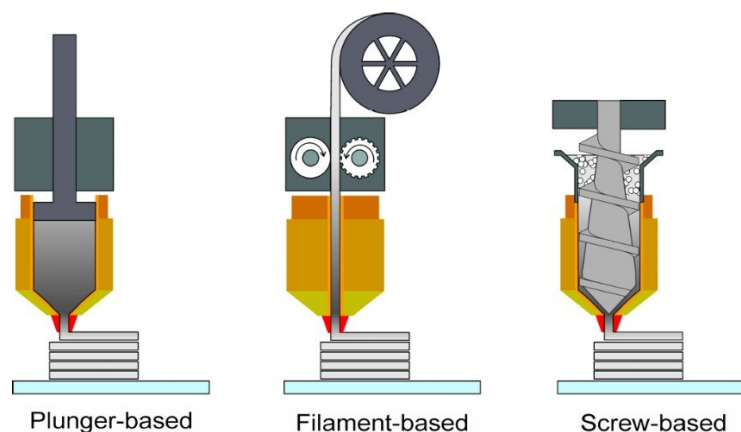


Fig. 2 Types of extruder used in MEX. Plunger-based (left), filament-based (middle), screw-based (right) [13]

The process for the plunger-type extruder starts by inserting profiles into cartridges. These are then passed into a plasticizing unit, where the thermoplastic material is heated until it reaches the desired softness for extrusion. The soft material accumulates in a storage area, and subsequently, a mechanical propulsion mechanism, like a plunger, releases the material. The 3D structure is formed by depositing it onto the building platform in multiple layers over time [13].

The screw extruder operates uniquely, divided into distinct zones. At first, in the solid conveying zone, pellets are transported to the melting zone. Here, they transform by the application of heat and friction. Next, in the metering zone, the molten material undergoes intense pressure before being extruded through the nozzle. The screw inside the extruder rotates and functions as a pump, transferring the material from the feeding zone to the nozzle [13].

The FDM process was patented and commercialized by Stratasys. The starting material are thermoplastic polymers, usually in a wire-like form, also known as filament, therefore the process is also called Fused Filament Fabrication (FFF). The coiled filament is fed into the heating area via a pushing mechanism of two counter-rotating rollers. The heating element is used to heat and melt the polymer slightly above its melting point. During the MEX process, the unmelted filament acts as a piston on the melted filament and pushes it out of the nozzle. After exiting the nozzle at the predetermined location, it bonds with the underlying layer and immediate cooling of the polymer takes place [9, 13].

Through this local application to a build platform or already solidified material, the object is built up in points or layers. MEX printers usually work in 3 axes, making it possible to produce 3D structures. While a layer is being applied, the print head can move in two axes in the x and y direction parallel to the print platform. As soon as a layer is applied, the print head can move upwards in the z-axis and start a new layer, or the platform moves down. For protruding components, support structures are required which can be removed during finishing. Furthermore, a post-processing procedure can be started to enable an improvement of the surface quality [9].

2.2 Metal Material Extrusion

Compared to conventional material extrusion, metal material extrusion involves the additional production steps of debinding and sintering. An overview of the process steps can be seen in Fig. 3.

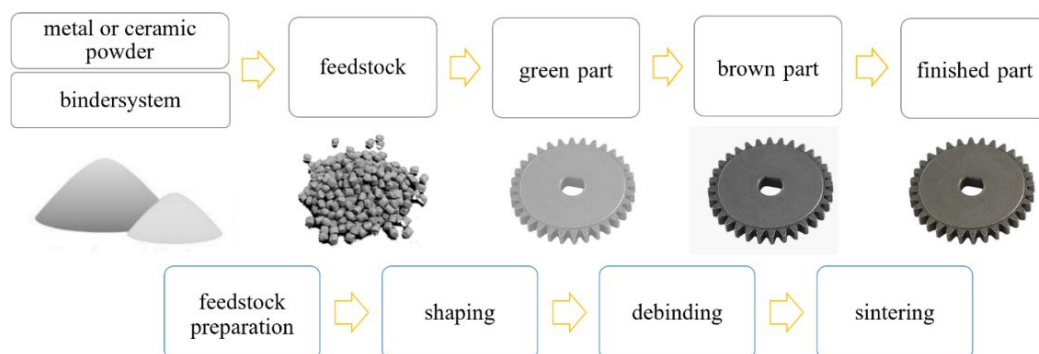


Fig. 3 Overview of processing steps SDS [21]

2.2.1 Feedstock Preparation - Compounding of a Multimaterial

In Material Extrusion (MEX) 3D printing, especially when using multiple materials, the creation of feedstock through compounding is an essential initial process. This process is crucial to ensure that the physical properties and quality of the final printed items meet requirements. Compounding improves the dispersion of filler particles in the polymer matrix, resulting in enhanced interaction between the surface area of the powder and the matrix. This interaction is vital for the material's overall performance. The interaction between the matrix and the

metallic fillers, as well as the processing parameters during melt compounding, play a crucial role in determining the quality of dispersion. A stronger affinity between the components leads to improved dispersion. Compounding can be done in two ways: continuous or batch-based. Continuous processes are often favored for industrial-scale production because of their efficiency. Continuous compounding machines include co-rotating twin screw extruders and Buss kneaders. On the other hand, batch compounders may use roller mills and high-shear internal mixers. The decision between continuous and batch compounding will be determined by the specific requirements and scale of the feedstock production. For this research, a high-shear internal mixer was utilized [12, 13].

The feedstock utilized in the SDS process consists of multiple components, including a binder system, a sinterable powder, and various additives. The binder system has a significant impact on both the manufacturing process and the quality of the final sintered parts, even though it is removed during the debinding stage. This system usually consists of various polymers, waxes, and additives, which are categorized into three main groups: the main binder component, the backbone, and the additives. The main binder component is the most voluminous and is the initial one to be eliminated during the debinding process. The backbone helps to preserve the part's shape during the initial debinding process and is then thermally decomposed before sintering. Additional components, such as dispersants and stabilizers, play a vital role in ensuring that filler particles are evenly distributed throughout the feedstock. However, no additives were utilized in the various feedstock formulations in these experiments [12, 13].

2.2.2 Filament Making

An essential stage in ensuring the high quality of the parts produced by MEX is the extrusion that creates the filaments used in MEX. The cross-section of the filament must be circular so it can be fed into the liquefier in the extrusion head. The filament's ovality, a measurement of how round it is, should be equal to zero. Additionally, the filament should have a very narrow distribution of diameters, goal 1.75 mm, over the length. Variations in the diameter cause underflow, which can lead to inadequate contact between adjacent deposited strands, creating weak points, or severe underflow, where there may not be any contact between the deposited strands, leading to voids between the strands, which in turn makes the parts less strong in terms of their mechanical performance. Overflow and material buildup near the nozzle are risks associated with filaments with too large diameters.

The high-pressure capillary rheometer (HPCR) equipped with a die of 1.75 mm can produce filaments. In general, this process does not produce high-quality filaments. However, due to the small amount of filaments required for the material tests, the HPCR was used to produce the filaments for these trials.

Using a single screw extruder equipped with a circular die is preferable for producing continuous filaments. In a water bath or on a conveyor belt, the extrudate is also cooled before being transported to the haul-off unit and then the winding unit. When producing bigger quantities of filaments, this technique is employed [12].

2.2.3 Shaping - Printing

The general filament printing process is described in section 2.1.1.7.

Precise control over the printing parameters is important for ensuring the quality and integrity of sintered parts. This must be tailored to the printer system, feedstock, and the specific shape and size of the printed part. For the production of flawless components with the desired sintered density, it is crucial to fine-tune various parameters. These include nozzle and build platform temperatures, the number of perimeters, infill pattern and density, printing speed, flow rate multiplier, and layer thickness.

Especially accurate control of the nozzle and build platform temperature is crucial for achieving optimal mechanical properties and dimensional accuracy. Higher temperatures typically result in improved adhesion between strands and less warpage due to shrinkage when solidifying. Printing temperatures can vary between 80 to 260 °C and are affected by various factors such as the binder type, metal powder, solid loading, and printing speed. Feedstock with a water-soluble binder typically requires a lower printing temperature compared to those that undergo solvent or thermal debinding. The build platform temperature is usually adjusted within a range of 40 to 100 °C to improve adhesion and reduce the occurrence of warping defects. In addition, the arrangement and thickness of the infill and the quantity of perimeters play a significant role in determining the strength and structure of the component. The printing speed and flow rate multiplier are important factors to consider; an incorrect flow rate can lead to problems like filament buckling. Thus, these parameters play a crucial role in defining the ultimate properties of the 'green' part, which refers to its state before debinding and sintering [13, 18, 28].

2.2.4 Debinding

Debinding is an essential step in Metal Extrusion Additive Manufacturing (MEX) and Metal Injection Molding (MIM) to guarantee the final sintered product's integrity and quality. While the binders employed in MEX and MIM exhibit similarities or occasional variations, their debinding stages demonstrate a very similar nature. The primary aim of the debinding phase is to facilitate the transformation of the 'green' component, which encompasses the polymer binder, into a 'brown' component, characterized by a framework of metal particles that are prepared for the process of sintering. The presence of any binder remains particularly carbon residues can have a negative effect on the sintering process and the overall quality of the end product, making this step necessary to optimize. Defects such as bloating, blistering, surface cracking, and internal voids may arise as a result of insufficient debinding.

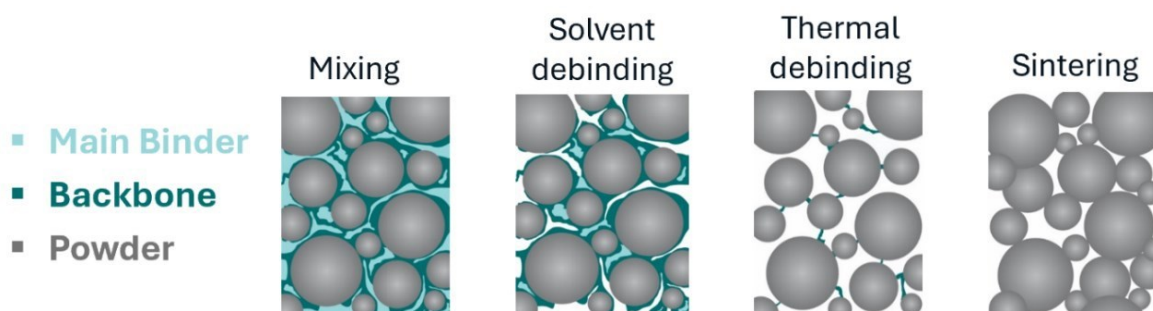


Fig. 4 Binder content during the SDS process steps [13]

Three principal methods - solvent, catalytic, and thermal processes - can be used for debinding. Thermal debinding is the predominant technique, which subjects the part to heat in order to melt and flow out or to thermally degrade the binder, causing it to diffuse out. The determination of the particular temperatures for this process is based on the composition of the binder. The process of solvent debinding, on the other hand, dissolves the binder by a solvent. Temperature, time, and the physical features of the particles have an impact on the rate at which the binder is dissolved. In contrast, the process of catalytic debinding utilizes acid vapors such as nitric or oxalic acid to degrade the primary binder at comparatively lower temperatures, approximately 120 °C. This approach aids in the reduction of thermal imperfections and applies to binders such as polyoxymethylene (POM), a polyacetal binder. Catalytic debinding has in the case of POM significantly higher efficiency compared to conventional thermal or solvent debinding techniques.

The process of debinding often consists of two separate phases, the primary debinding phase and the secondary debinding phase. The primary debinding phase of the process involves the elimination of the soluble binder constituent, often achieved through solvent debinding, resulting in the formation of a porous framework that is essential for the secondary phase. This setup enables a more convenient extraction of the polymer backbone during the process of thermal debinding. However, the process of solvent debinding requires a delicate equilibrium, as inadequate elimination may result in imperfections such as bloating, while excessive removal may jeopardize the structural integrity of the component. Bloating is a phenomenon that arises in regions with a high concentration of binder, where the vapor is unable to readily escape. Consequently, the partial pressure of the trapped vapor surpasses the air pressure, leading to the formation of bubbles. The second debinding phase involves subjecting the material to thermal treatment in order to eliminate the residual backbone binder. This phenomenon commonly takes place at elevated temperatures, spanning from 200 °C to 600 °C, dependent upon the composition of the backbone. The pace at which the dissolved polymer is extracted, which involves dissolution and diffusion, is influenced by various elements such as temperature, duration, and the particle properties of the item being treated.

The efficacy of these techniques ultimately depends on their capacity to efficiently eliminate the binder while maintaining the integrity of the component's structure, resulting in a robust metallic framework that is prepared for the sintering procedure. The choice of debinding process, whether it is solvent, catalytic, or thermal, should be determined by the composition of the binder and the specific needs of the manufactured component. In this experiments, a two-step debinding process was chosen with the combination of solvent debinding as the primary phase and thermal debinding as the second phase [13, 14, 16, 28, 30, 32].

2.2.5 Sintering

The sintering process represents the last process step in SDS and plays a crucial role as a thermal treatment that consolidates metallic powders into bulk materials. Sintering improves the mechanical strength of the material, while often resulting in the presence of residual porosity. In the process of sintering, the primary component of the metal or ceramic powder is subjected to temperatures below its melting point, typically ranging from 70 to 90 % of the melting temperature. At higher temperatures, metal particles undergo recrystallization without undergoing melting, facilitating their fusion via solid-state atomic diffusion. This is subsequently followed by recrystallization and the establishment of grains. The process of neck growth between particles in consolidated powders is facilitated by several mass transport mechanisms, including surface diffusion, evaporation-condensation, grain boundary diffusion,

lattice diffusion, viscous flow, and plastic flow. These mechanisms contribute to the enhancement of the strength of the consolidated powders. Some of the mechanisms result in a size reduction between 10 – 20 %.

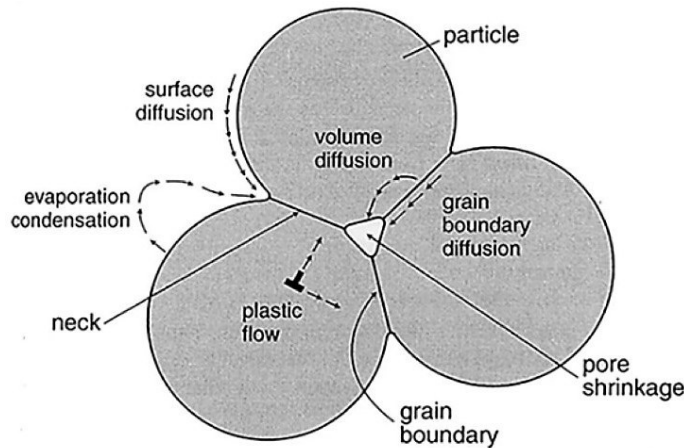


Fig. 5 Sintering of three particles, showing possible paths of the atomic motion involved with neck growth and densification [7]

In addition to utilizing heat to facilitate diffusion and mass transport processes, the sintering process has distinct stages that influence the ultimate microstructure and characteristics of the components. At first, the porous structure is open and interconnected, and as the temperature increases, necks form at the sites where particles come into contact. During the intermediate phase, a range of mass transport systems plays a role in the expansion of the neck, resulting in a decrease in porosity and an increase in densification. Ultimately, during the final phase, the process causes the pores to reduce in size and transform into circular and isolated structures, leading to densification. Prolonged sintering can lead to an increase in grain size, which can have a negative impact on mechanical characteristics [2, 7, 14, 29].

The decrease of surface energy is a crucial aspect of the sintering process since it involves minimizing the surface area. This is accomplished by reaching the diffusion activation energy, which triggers the development of cohesive bonds or necks between particles. The process is facilitated by the small particle sizes, which possess high surface areas, as well as the pressure differences between concave and convex bonds. The microstructure and characteristics of the final part, which can achieve relative densities up to 98 %, are significantly influenced by parameters such as heating and cooling rates, time at the sintering temperature, and the environment of the process. The solid-state densification technique demonstrates the profound correlation between processing conditions and the ultimate characteristics of sintered materials, as it successfully converts 'brown' components into final, densely packed pieces. The approximate sintering temperature of aluminum is 550 °C [7, 14, 29].

3 Hypotheses and Approach

3.1 Hypotheses

The backbone serves as the foundation of the binder systems, while a main binder for example, a thermoplastic elastomer (TPE), promotes flexibility and serves as a soluble component of the binder system. To maintain the shape of the components during debinding, the backbone should have high chemical resistance to the solvent, whereas the soluble part should dissolve during the first stage of debinding. All of the different types of backbones were selected to improve the mechanical properties required for MEX and powder dispersion.

Hypothesis 1: The hypothesis suggests that the addition of maleic anhydride (MA) to polyolefine, such as HDPE-MA and PP-MA, can improve the adhesion between the polymer and metal particles. This is because MA can promote stronger polar contacts. As a result of this, the wetting of the metal powder is expected to improve, resulting in a feedstock material that has a lower viscosity, better mechanical strength, and less formation of agglomerates. Ultimately, this will lead to the production of parts with superior quality and fewer flaws during the sintering process.

3.1.1 Cyclohexane Debinding Binder System

Hypothesis 2: The use of binder system type 1 (PLA+TPE 1) is expected to improve the thermal debinding behavior due to the low thermal degradation of PLA (~380 °C complete decomposition) [20]. The lower debinding temperature facilitated by PLA is advantageous considering the low sintering temperature of aluminum, thereby enhancing the overall process efficiency.

Hypothesis 3: TPE 1 is anticipated to improve the quality of the brown part by reducing the residue amount after solvent debinding [15]. The inclusion of TPE 1 in the binder system is expected to result in lower carbon residue diffusion during sintering, which may otherwise cause sintering problems and adversely affect the microstructure.

3.1.2 Acetone Debinding Binder System

Hypothesis 4: The incorporation of a thermoplastic elastomer TPE 4 with different shore hardness in the binder system (TPE 4/PP-MA and TPE 4/HDPE-MA) is projected to enhance the flexibility of the filament. Additionally, the TPE 4's acceptable thermal behavior contributes to favorable conditions during the thermal debinding step.

3.1.3 Water Debinding Binder System

Hypothesis 5: The hypothesis suggests that Polyvinyl Alcohol (PVA) can be used as the primary binder component due to its high solubility in water, which could provide a more ecologically friendly alternative to acetone and cyclohexane for solvent debinding purposes.

3.2 Approach

The primary objective of this master's thesis was to conduct a thorough examination and optimization of the feedstock formulations for aluminum additive MEX. The study primarily targeted in conducting a comprehensive evaluation of nine different binder systems, analyzing their processing procedures and performance outcomes. In this study, four main binder components, namely TPE 1, ASA, TPE 4 and PVA, were chosen based on their compatibility with certain debinding solvents. Additionally, TPE 4 was available in three separate shore A hardness grades (20 A, 40 A and 70 A), each of them was compared and analyzed. Cyclohexane was picked as a solvent for TPE. ASA and TPE 4 were chosen for acetone, and water for PVA. In addition, the influences of different backbone materials were investigated on the quality of samples during the SDS process, employing an analytical methodology to analyze four volume fractions (25, 30, 35, and 40 vol.%) for each binder system. An aluminum powder content of 55 vol.% was defined for all binder formulations. The formulations were compared according to their thermal, mechanical, rheological, printing and debinding characteristics, thus providing a comprehensive understanding of their effectiveness in the field of MEX.

Four fundamental steps define the research approach and the overview of the aspects investigated and the information gained in each process step can be seen in Fig. 6.

Phase 1 commence with the production of 36 feedstock formulations, which were subsequently subjected to post-kneading and grinding processes to transform them into filaments. Initial printing experiments employed simple and easily printable test shapes to evaluate the capacity to print and maintain shape after debinding, while also identifying the best printing conditions for each binder system.

In **Phase 2**, the focus was on assessing the thermal properties of the formulations using Differential Scanning Calorimetry (DSC) and Thermogravimetric Analysis (TGA), as well as examining their rheological properties. For this analysis, additional binder material without powder was prepared with the kneader. The assessment stage plays a crucial role in finding formulations that possess the most favorable characteristics for subsequent optimization.

Phase 3 involved the submission of formulations that demonstrate favorable outcomes to the project partner IFAM for a comprehensive evaluation of their debinding and sintering characteristics. The purpose of this cooperation phase was to enhance the understanding of material behavior during debinding and sintering settings.

Phase 4 of the research entailed conducting tensile testing on the sintered components to determine their final mechanical characteristics. The completion of this ultimate stage was crucial in confirming the effectiveness of the optimized binder systems and formulations in generating end-products that possess exceptional mechanical strength.

The approach of the work was to analyze and compare 9 different binder systems. As a main binder component, the following polymers, TPE 1, ASA, TPE 4 and PVA, depending on the solvent, have been chosen. For TPE cyclohexane will be used for debinding. ASA & TPE 4 was dissolved in acetone and PVA in water. The influence of the different backbones on sample quality during the different process steps was compared. In the first phase, four-volume fractions were chosen for each binder system. The volume fraction of the backbone was 25,

30, 35, and 40 vol.%, the soluble part was calculated according to the selected volume percentages for the backbone. The aluminum powder content is fixed at 55 vol.%. The thermal, mechanical, and rheological properties of the binder system will be determined and the binders will be compared with each other.

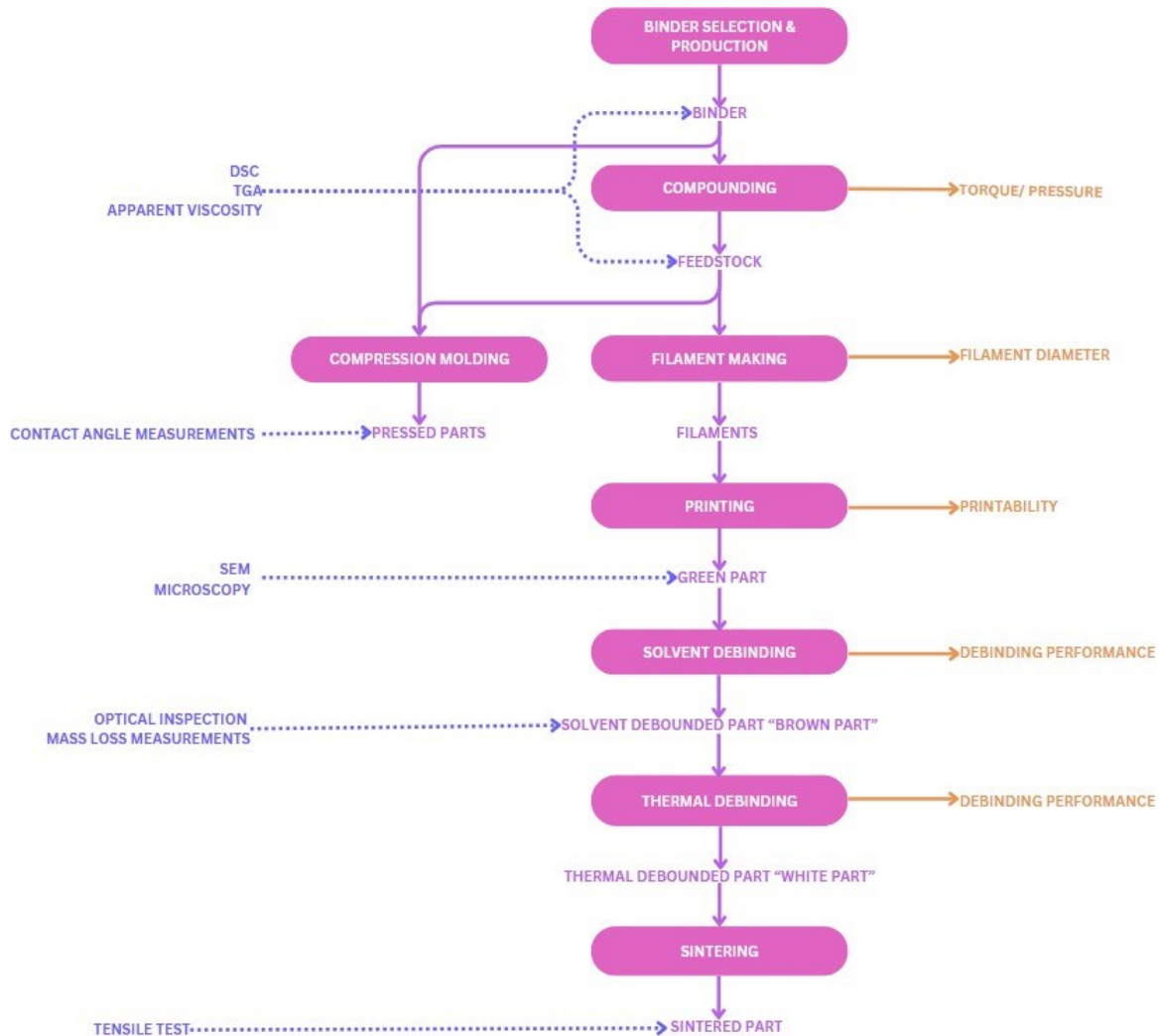


Fig. 6 Process steps of the SDS process with an overview of which aspects were investigated and which information could be gained

4 Materials and Methods

4.1 Materials

A spherical aluminum (AlSi1 99 % aluminum and 1 % silicon) alloy powder with a particle size distribution where 90 % of the particles are smaller than 32 μm ($d_{90} < 32 \mu\text{m}$) was used to create feedstocks for MEX. The AlSi1 powder was obtained from TLS Technik Spezialpulver KG in Bitterfeld-Wolfen, DE. Each formulation for the feedstocks was prepared with a consistent powder content of 55 vol.% and included a two-component binder systems with varying backbone contents of 25, 30, 35, and 40 vol.%. The volume percent of the main binder component in each formulation is determined numerically using the given volume fraction of the backbone component. This methodology enables a systematic study of how changes in backbone content affect the processability and mechanical properties of MEX feedstocks and allows for the comparison of different compositions of binder systems.

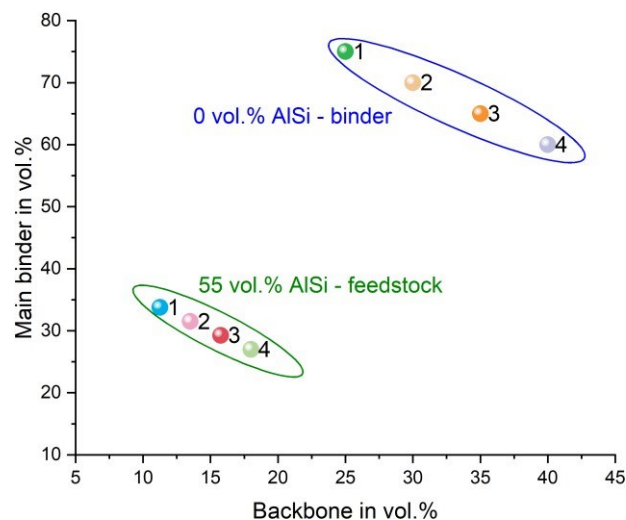


Fig. 7 Overview binder and feedstock formulations

The following feedstock and binder systems are listed in Table 2 and the specifications for the production of the sample are explained in detail under 4.2.

This work involved the selection of multiple main binder materials like the thermoplastic elastomers, TPE 1, and TPE 4, the thermoplastic polymers, Acrylonitrile Styrene Acrylate (ASA), and Polyvinyl alcohol (PVA). As backbones the polyolefin, High Density Polyethylene (HDPE-MA) and Polypropylene (PP-MA), as the thermoplastic, thermoplastic polyester elastomer (TPC), TPE 3, ethylene butyl acrylate copolymer (TSEB); Polylactic Acid (PLA), and ASA were selected. TPE 4 was available in three separate shore A hardness grades (20 A, 40 A and 70 A). Both polyolefines, HDPE-MA and PP-MA, were combined with the three different TPE 4 to create an acetone debinding feedstock and with TPE 1 for a cyclohexane debinding feedstock. The three different shore A hardness grades of TPE 4 were chosen to determine if a particular hardness significantly improves the flexibility of the filament and there for, the handling during the printing process.

Table 2 Overview Formulation Composition and Sample names

	Backbone	Vol. %	Main Binder	Vol. %	Powder	Vol. %	Sample name				
Cyclohexane	PLA	11.25	TPE 1	33.75	AlSi1	55	PLA(H)_55_1				
		13.50		31.50			PLA(H)_55_2				
		15.75		29.25			PLA(H)_55_3				
		18.00		27.00			PLA(H)_55_4				
		25.00		75.00			0	PLA(H)_0_1			
		30.00		70.00				PLA(H)_0_2			
		35.00		65.00				PLA(H)_0_3			
		40.00		60.00				PLA(H)_0_4			
	PP-MA	11.25		33.75		55	PP(H)_55_1				
		13.50		31.50			PP(H)_55_2				
		15.75		29.25			PP(H)_55_3				
		18.00		27.00			PP(H)_55_4				
		25.00		75.00			0	PP(H)_0_1			
		30.00		70.00				PP(H)_0_2			
		35.00		65.00				PP(H)_0_3			
		40.00		60.00				PP(H)_0_4			
	HDPE-MA	11.25		33.75		55	HDPE(H)_55_1				
		13.50		31.50			HDPE(H)_55_2				
		15.75		29.25			HDPE(H)_55_3				
		18.00		27.00			HDPE(H)_55_4				
		25.00		75.00			0	HDPE(H)_0_1			
		30.00		70.00				HDPE(H)_0_2			
		35.00		65.00				HDPE(H)_0_3			
		40.00		60.00				HDPE(H)_0_4			
	Acetone	PP-MA		15.75		TPE 4 20 A	29.25	55	55	PP(AC)_55_1	
						TPE 4 40 A				PP(AC)_55_2	
						TPE 4 70 A				PP(AC)_55_3	
				35.00		TPE 4 20 A	65.00		0	PP(AC)_0_1	
TPE 4 40 A			PP(AC)_0_2								
TPE 4 70 A			PP(AC)_0_3								
HDPE-MA		15.75	TPE 4 20 A	29.25	55	55	HDPE(AC)_55_1				
			TPE 4 40 A				HDPE(AC)_55_2				
			TPE 4 70 A				HDPE(AC)_55_3				
		35.00	TPE 4 20 A	65.00		0	HDPE(AC)_0_1				
			TPE 4 40 A				HDPE(AC)_0_2				
			TPE 4 70 A				HDPE(AC)_0_3				
TPC		15.75		29.25	55	55	TPC(AC)_55_1				
TPE 3							TPE 3(AC)_55_1				
TSEB		11.25		ASA	33.75	55	55	ASA(AC)_55_1			
								13.50	31.50	ASA(AC)_55_2	
								15.75	29.25	ASA(AC)_55_3	
								18.00	27.00	ASA(AC)_55_4	
								25.00	75.00	0	ASA(AC)_0_1
								30.00	70.00		ASA(AC)_0_2
								35.00	65.00		ASA(AC)_0_3
								40.00	60.00		ASA(AC)_0_4
H ₂ O		ASA	15.75	PVA	29.25	55	55	ASA(H2O)_55_1			
		TSEB						TSEB(H2O)_55_1			
		PLA						PLA(H2O)_55_1			

The polyolefines, PP-MA and HDPE-MA, were chosen as backbones because they are non-soluble in cyclohexane and acetone as well as their chemical structure. HDPE-MA and PP-MA because of, are both polyolefines grafted with maleic anhydride (MA), which improves the direct contact of the polar components with metal particles, resulting in enhanced adhesion between the metal and the polymer binder matrix. The improved adhesion limits the mobility of polymer chains, resulting in higher viscosity and strength. Furthermore, it aids in decreasing the formation of powder agglomerates, which can potentially reduce the occurrence of defects in components during the debinding process.

PLA, Polylactic Acid, a biodegradable polymer has been chosen as the backbone for a cyclohexane-based feedstock, along with TPE 1 as the main binder, to investigate its thermal degradation temperature compared to PP-MA and HDPE-MA. The focus on thermal degradation temperature is vital, particularly considering the low sintering temperature of AISi1. Reducing the thermal degradation temperature of the binder system may significantly enhance the quality of the sintered parts.

ASA, Acrylonitrile Styrene Acrylate, is an amorphous thermoplastic notable for its mechanical properties and solubility in acetone. This ability of solubility in acetone is already used in MEX as a postprocessing step to improve printed ASA surfaces by allowing for the creation of smooth and glossy finishes. To further enhance the versatility and performance of the feedstock, ASA is combined with thermoplastic elastomers as the backbone materials to improve the flexibility of the formulation. TSEB, an ethylene butyl acrylate copolymer also functionalized with maleic anhydride, is used as a backbone in combination with ASA as an acetone-based feedstock system. Other backbones, TPC and TPE 3, are compared as an alternative for TSEB. TPC, a thermoplastic polyester elastomer, and TPE 3, which is a styrenic thermoplastic elastomers are chosen as a comparison because both should provide good flexibility at low temperatures.

To develop a more sustainable alternative to solvents such as cyclohexane and acetone, PVA was selected as the main binder for water-soluble feedstock formulations, along with ASA, TSEB, and PLA as backbones. Polyvinyl alcohol (PVA) is very desirable due to its high water solubility, making it ideal for printing applications where it is used to produce removable structural supports. Nevertheless, the high moisture absorption of PVA requires pre-drying, and it is susceptible to thermal aging, which poses issues during the printing process.

The material properties of the binder components are listed in Table 3.

Table 3 Overview of material properties

Type	Material	MFR in g/min	Density in g/cm ³
Main binder Polymers	TPE 1	-	0.940
	TPE 4 – 20 A	>100 @190 °C @ 5 kg	0.890
	TPE 4 – 40 A		
	TPE 4 – 70 A		
	ASA	12 @ 220 °C @10 kg-	1.070
	PVA	-	1.230
Backbone Polymers	HDPE-MA	1-4 @190 °C @ 2.16 kg	-
	PP-MA	6.37 @190 °C @ 2.16 kg	0.935
	PLA	35 @190 °C @ 2.16 kg	1.237
	TPC	25 @240 °C @ 2.16 kg	1.11
	TSEB	3 @190 °C @ 2.16 kg	-
	TPE 3	70 @230 °C @ 2.16 kg	0.910
Powder	AlSi1	d90 < 32 µm	

4.2 Preparation of Compounds

The binder and feedstock were carefully mixed using an internal mixer that had a chamber volume of 38 cm³ and counter-rotating roller rotors (Haake 600 Rheomix, Thermoscientific™ Waltham, MA USA). The procedure was conducted under controlled conditions, with a temperature depending on the material between 175 °C and 200 °C, a rotational speed of 60 rpm, and an air atmosphere, for a length of 45 minutes. The specified duration was specifically selected to provide an ideal distribution of powder particles inside the binder system. This was confirmed by the attainment of a consistent torque value at the end of the mixing process. To maintain methodological consistency and facilitate comparative analysis, all binder systems, except for PLA, underwent the same processing conditions for a length of 45 minutes see Table 4.

A different processing methodology was implemented for formulations that included Polylactic Acid (PLA) as a component, in comparison to the normal procedure. Because PLA is prone to thermal damage when exposed to high temperatures for a long time, the overall mixing duration was intentionally lowered to 25 minutes. The PLA material itself was mixed for a shorter length of 15 minutes. This adjustment was performed to reduce the risk of material degradation, ensuring the strength and quality of the PLA in the feedstock or binder systems. After the mixing phase, the feedstocks were cooled to room temperature and then granulated using a cutting mill (SM200, Retsch GmbH, Haan, DE).

Table 4 Comparison of compounding programs with and without PLA in the formulation

Time in min	t=0	t=3	t=8	t=13	t=18	t=45
Formulations without PLA	Main Binder	AlSi1				End
	Backbone					

Time in min	t=0	t=2	t=2	t=6	t=8	t=10	t=25
Formulations with PLA	Main Binder	AlSi1			Backbone (PLA)	End	

4.3 High-pressure capillary rheometer Rheograph 2002 Göttfert

Using a high-pressure capillary rheometer (HPCR), Rheograph 2002 (GÖTTFERT Werkstoff-Prüfmaschinen GmbH, Buchen, DE), the viscosity was determined. From these values, conclusions can be drawn about the processability of the different compositions for subsequent additive manufacturing. In the rheometer, the plastic granulate is filled into the cylinder and melted by heat conduction. A hydraulically operated piston, moving at a speed of 0.5 mm/s, suitable for the production of filaments, presses the plastic melt through a round nozzle at the bottom of the cylinder. A round nozzle with a diameter of 1.75 mm was installed in the HPCR. With the GAL-25 conveyor belt from Geppert-Band GmbH (Jülich, DE), the plastic melt was cooled, and filaments were produced. These process steps provided a straightforward method for filament production for the material compositions under investigation.

In the rheometer, the apparent shear rate $\dot{\gamma}_{ap}$ (1) and the apparent shear stress τ_{ap} (2) can be calculated from the measured pressure drop, the geometry of the round nozzle, and the volume flow rate. The pressure drop was recorded at six to ten time steps with a pressure transducer. The apparent viscosity η_{ap} (3) of the melt is calculated from the apparent shear rate and the apparent shear stress. The viscosity measurements were conducted three times for each binder and feedstock system.

$$\dot{\gamma}_{ap} = \frac{4 \cdot V}{\pi \cdot R^3} \quad (1)$$

$$\tau_{ap} = \frac{p \cdot R}{2 \cdot L} \quad (2)$$

$$\eta_{ap} = \frac{\tau_{ap}}{\dot{\gamma}_{ap}} \quad (3)$$

4.4 Debinding

The debinding procedure proceeded by accurately measuring the geometric dimensions and initial weight of the printed discs. This data served as a baseline for assessing material loss and any changes in geometry that may occur during the debinding process. Approximately five printed parts were analyzed for each formulation.

After performing the preliminary measurements, the debinding process was commenced by dividing the printed discs into two equal parts and submerging one-half into a container containing the appropriate solvent (cyclohexane, acetone, water) chosen depending on its compatibility with the binder material.

The debinding process was conducted for 24 hours at room temperature, which was considered adequate for the solvent to fully dissolve the primary binder constituent. Following the conclusion of this time frame, the solvent underwent an optical examination to identify any cloudiness or the existence of particles, which serve as signs of inadequate dissolution of the improper material and insufficient efficacy of the binder removal procedure.

Following the debinding process, the components were removed from the solvent and subjected to a 12-hour drying process in air at room temperature. Drying was carried out to remove any remaining solvent that could potentially impact later evaluations or compromise the integrity of the components. After the drying process, an optical examination was performed to detect any defects, such as cracks or other fractures, that might have occurred during the debinding procedure. This evaluation aimed to determine the effect of debinding on the structural integrity of the components.

The final stage of the debinding procedure entailed the quantification of the mass of the part after the debinding process. The quantification of mass reduction Δm , which can be attributed to the removal of the main binder constituent, was accomplished through a comparison of the initial and final masses of the printed disks. The quantitative assessment functioned as a measure of the efficacy of the debinding procedure.

$$\Delta m = \frac{m_1 - m_2}{m_1} \cdot \frac{1}{\varphi_m} \cdot 100\% \quad (4)$$

The variables in the equation are defined as follows: m_1 represents the initial mass before the debinding process, m_2 represents the final mass, and φ_m represents the mass fraction of the main binder.

4.5 DSC

The thermal properties, encompassing both the melting and cooling behavior of the binder systems and feedstocks, were thoroughly analyzed using a Differential Scanning Calorimeter (DSC) manufactured by Mettler Toledo GmbH, Greifensee, CH. In this investigation, duplicates of each type of binder and feedstock without any prior drying procedure were investigated. A temperature range of 25 to 250 °C was chosen. The procedure employed a heating rate of 10 K/min and a cooling rate of 20 K/min, in the presence of a nitrogen environment with a gas flow rate of 50 ml/min. The glass transition temperature, melting temperature, and crystallization temperature of the binder systems were established as key thermal parameters. Approximately 15 mg of the samples were placed in perforated differential scanning

calorimetry (DSC) crucibles for accurate measurement. Table 5 describes the program employed. Each formulation was analyzed twice.

Table 5 DSC program overview

Sample mass	Heating curve				Cooling curve	
	Start temperature	Holding time	Heating rate	End temperature	Holding time	Cooling rate
~15 mg	25 °C	0	10 K/min	250 °C	0	20 K/min

The degree of crystallinity X_c in the polymer and binder system was calculated using equation (5), whereas for PLA, due to its cold crystallization characteristics, equation (6) was employed.

$$X_c = \frac{\Delta H_m}{\Delta H_m^0} \cdot \frac{1}{\varphi_m} \cdot 100\% \quad (5)$$

$$X_c = \frac{\Delta H_m - \Delta H_c}{\Delta H_m^0} \cdot \frac{1}{\varphi_m} \cdot 100\% \quad (6)$$

Where ΔH_m is the enthalpy of melting, ΔH_c is the enthalpy of crystallization, φ_m is the weight fraction of the crystalline polymer and ΔH_m^0 is the enthalpy of the 100% crystallized polymer in the sample, which is 93.7 J/g for PLA [31], 207 J/g for PP and 293 J/g for HDPE [4].

4.6 TGA

To assess the thermal stability of binder systems and feedstocks, thermogravimetric analysis (TGA) was conducted using equipment from Mettler Toledo GmbH, Greifensee, CH. This approach attempted to quantify the variations in sample weight, expressed in weight percent (wt.%), in response to changing temperatures within an inert nitrogen atmosphere. A single test was performed for each sample, in which the temperature was gradually raised from ambient temperature to 800 °C at a heating rate of 10 K/min. This methodology enables a comprehensive examination of the thermal degradation patterns of the materials, providing valuable information on how they react to high temperatures and the stability of the formulation. Each formulation was analyzed twice.

4.7 Contact Angle Measurements

The contact angles of the backbone and primary binder polymers were evaluated using discs produced via compression molding. The P200PV hydraulic vacuum press from (Collin Lab & Pilot Solutions GmbH, Maitenbeth, DE) was used for pressing the specimens. The procedure utilized a steel framework with a thickness of 2 mm and polished polytetrafluoroethylene (PTFE) plates to ensure uniform compression and maintain uniformity in surface roughness. The molding process parameters are displayed in Table 6.

Table 6 Process parameter compression molding contact angle discs

Process step	1	2	3
Time in min	5	15	20
Pressure in bar	1	75	
Temperature in °C	200		30

The contact angle measurements were performed on the pressed discs at ambient temperature using the Krüss DSA100 goniometer manufactured by Krüss GmbH, Hamburg, DE. Deionized water and diiodomethane were used as the testing liquids. Fifteen repetitions were conducted for each polymer-liquid combination to assure precision and dependability.

The contact angle can be determined by measuring a static drop, which remains at a fixed volume throughout the measurement, or by measuring a dynamic contact angle, where the angle is seen as the drop size fluctuates, continuously reforming the interface. This entails differentiating between the angle of approach and the angle of retreat. In this investigation, measurements were taken on the static contact angle, which indicates that the volume of the drop stayed constant during the measuring process. This decision emphasizes the importance of comprehending the inherent surface characteristics of the polymers when they are not in motion. The contact angle measurement helps gaining a better knowledge of how the material interacts with the test liquids and clarifies whether they are more hydrophobic or hydrophilic.

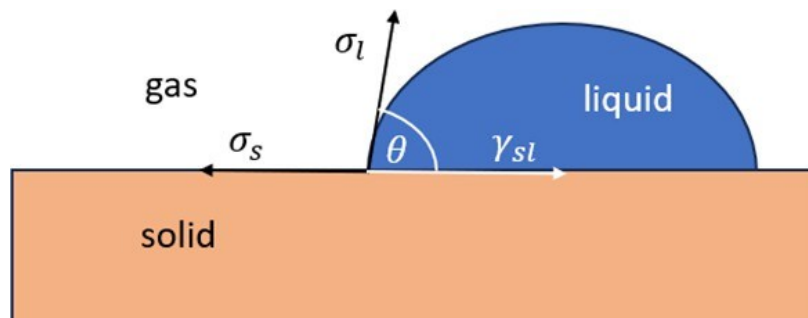


Fig. 8 Contact angle formation on a solid according to Young [33]

Young formulated the relationship between the contact angle θ and the interfacial tension γ_{sl} based on a three-phase contact line. See Equation (5) and Fig. 8 [33].

$$\sigma_s = \gamma_{sl} + \sigma_l \cdot \cos\theta \quad (7)$$

According to the Owens, Wendt, Rabel and Kaelble (OWRK) method, the surface tension of each phase can be divided into a polar (σ_s^p, σ_l^p) and dispersive (σ_s^d, σ_l^d) part. The indices s and l indicate a solid and liquid phase and the surface tension is indicated with the symbol σ [17, 23].

$$\sigma_l = \sigma_l^p + \sigma_l^d \quad (8)$$

$$\sigma_s = \sigma_s^p + \sigma_s^d \quad (9)$$

Owen and Wendt defined according to the previous equations (7-9) and assumptions the following Equation (8) for the interfacial tension [23].

$$\gamma_{sl} = \sigma_s + \sigma_l - 2 \cdot (\sqrt{\sigma_s^d \cdot \sigma_l^d} + \sqrt{\sigma_s^p \cdot \sigma_l^p}) \quad (10)$$

4.8 Printing

The printing procedure was carried out using the Prusa i3 MK3 FFF printer (Prusa Research, Prague, CZE), which has a nozzle diameter of 0.4 mm. The printing parameters were established as optimized parameters after conducting a series of trials. At least five samples were printed for debinding testing and to ensure a reliable result for comparing the printability of each feedstock system. The chosen geometry for the printing process is shown Fig. 9.

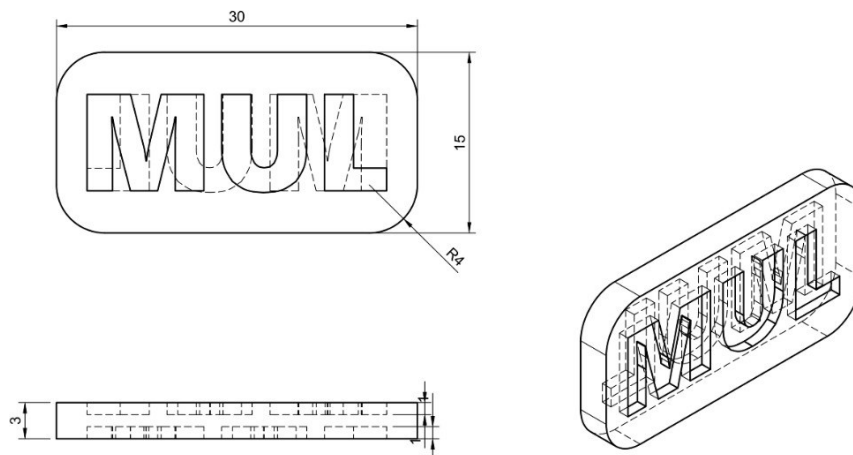


Fig. 9 Sample geometry for printing trials [22]

4.9 Morphology Analyses

The morphology of the AISi1 powder as well as the feedstock systems of the optimized binder system formulations was studied by a scanning electron microscope (SEM) from Tescan Vega II (Tescan Brno, CZ). The measurement was performed once on the grinded feedstock, to evaluate the particle distribution and the interfacial adhesion between the binder system and the AISi particles, at 2 kV and 5 kV using secondary electrons.

5 Results and Discussion

5.1 Evaluation of the Torque Measurements

The torque measurements (Fig. 11), single measurement curve, taken during the compounding process of HDPE(H)_1 and PP(H)_1 feedstocks show different behaviors depending on the binder system employed. In the case of grafted binder systems, the mixing torque does not reach a stable state during the mixing period. Instead, it consistently decreases over a duration of 45 minutes. On the other hand, the binder systems PP(H)_0 generate a consistent level of torque in a shorter period of time, in about 5 minutes. This observation indicates that the existence of AlSi1 particles in the feedstock requires more time for mixing in order to achieve a stable and constant final torque. This is likely because it is more difficult to evenly disperse these particles inside the polymer matrix, leading to higher complexity. Additionally, a comparison between PP(H)_55_1 and PP(H)_55_1_new shows the impact of temperature on the maximum torque value. Increasing the mixing temperature from 180 °C to 200 °C, decreases the final torque around from 11 Nm to 2 Nm.

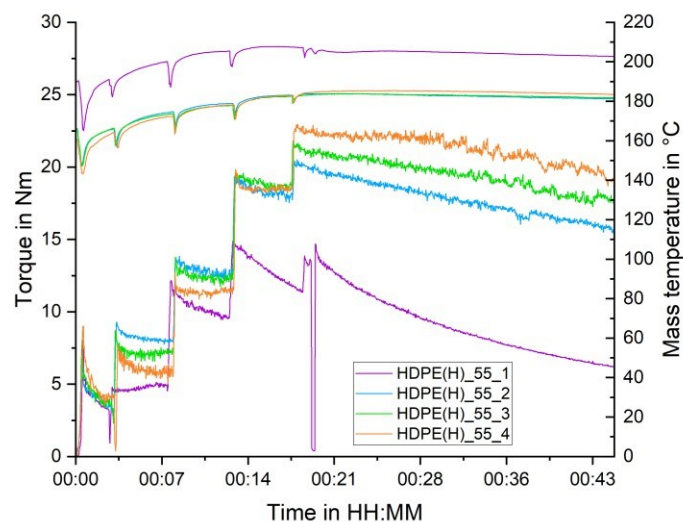


Fig. 10 Overview torque measurement HDPE(H)_55

In Fig. 10 can be seen, that after 25 minutes, a stable mixing torque is achieved for the HDPE(AC) formulation that can be debinded using acetone. However, in the case of PP(AC), see Fig. 11, and ASA(AC), there is a clear reduction in torque seen after 45 minutes.

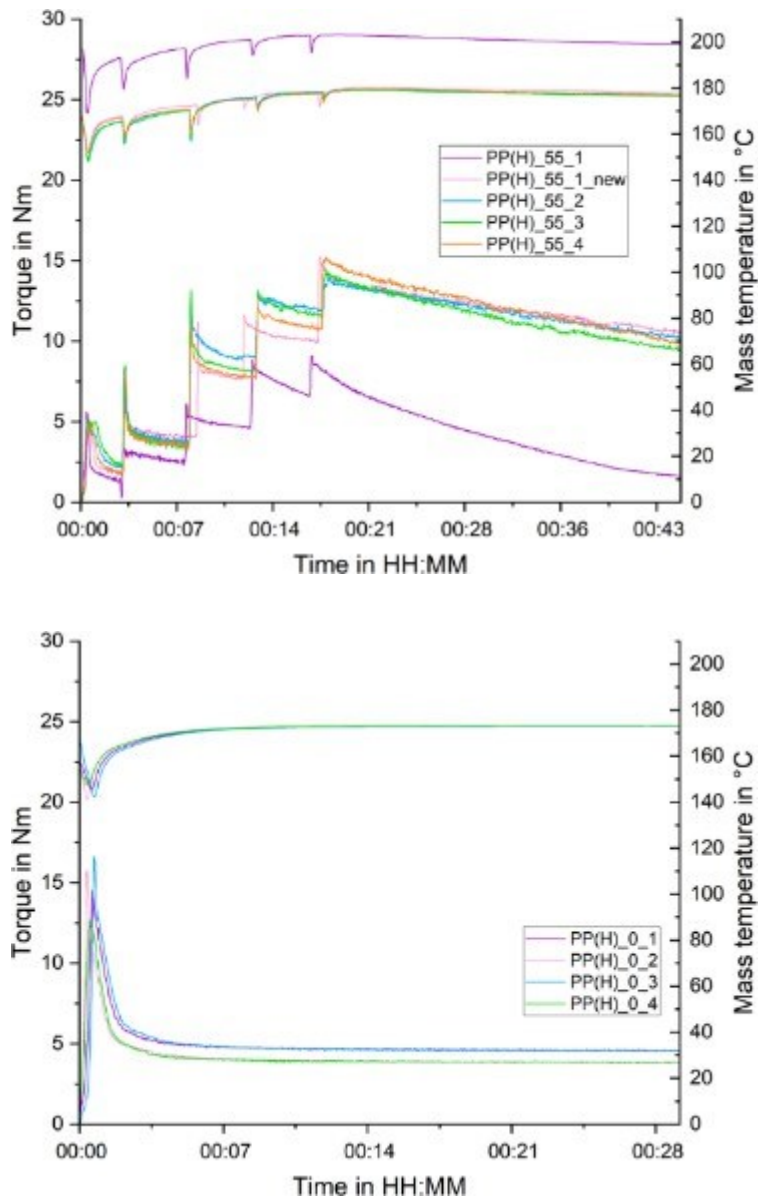


Fig. 11 Overview torque measurement curves PP(H)_55 (top), PP(H)_0 (bottom)

On the other hand, PLA(H) stands out with its remarkably short total mixing duration of 25 minutes compared to the other samples under study, to avoid thermal degradation. Due to this, the torque curve shows that the torque value remains at 0 Nm until 10 minutes, indicating that sufficient mixing and powder distribution begin only after the chamber reaches a certain fill level, after adding PLA. Additionally, the final torque remains decreasing as well.

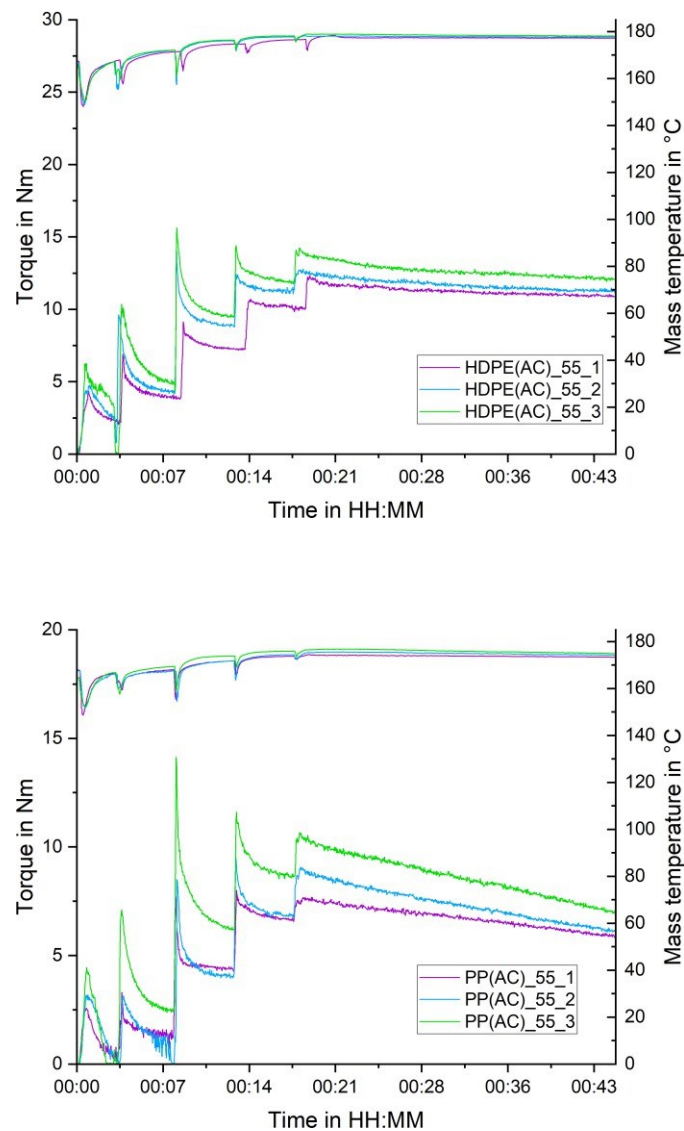


Fig. 12 Overview torque measurement curves HDPE(AC)_55 (top), PP(AC)_55 (bottom)

When comparing the final torques, the PP(AC) material possesses the lowest torque at 7.5 N·m. It is followed by PP(H), PLA(H), and HDPE(AC), which all have an average torque of approximately 11 N·m. ASA demonstrates the greatest ultimate torque, approximately 17.5 N·m, indicating a greater resistance to flow or a binder system with higher viscosity that could further affect processing and extrusion characteristics.

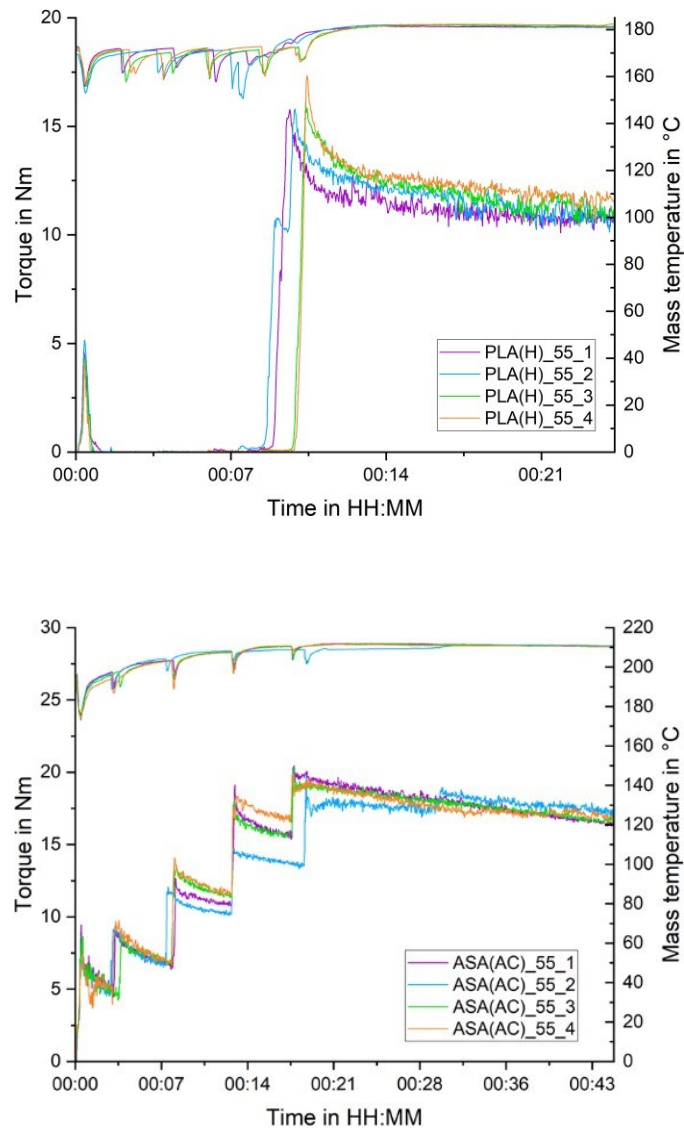


Fig. 13 Overview torque measurement curves PLA(H)_55 (top), ASA(AC)_55 (bottom)

In addition, the torque graphs for HDPE(H) and PP(H) demonstrate how the processing temperature affects the final torque. This suggests that both the composition of the feedstock and the processing parameters, such as temperature, are important factors in influencing the mixing behavior and the ultimate torque values.

5.2 Evaluation of the Viscosity

The rheological measurement with the HPCR aimed to evaluate the apparent viscosity over a range of shear rates spanning from 75 1/s to 1000 1/s. It can be noted that all the sample feedstocks, as well as the binder system, display shear-thinning behavior, which means that the viscosity decreases as the shear rate increases. This phenomenon highlights the non-Newtonian fluid properties of the materials being studied. In this case, the polymer chains of the materials entangle and align with the flow direction, resulting in a decrease in internal resistance and viscosity. Further can be observed from the viscosity data, that the feedstock, which consists of the binder system with a powder concentration of 55 vol.%, exhibits higher viscosity levels compared to the binder system alone. The rise in value can be ascribed to the interactions occurring between the aluminum particles and the polymer binder system, leading to a more restricted system. Within this particular environment, the mobility of polymer chains is considerably limited compared to that in the polymer without any AlSi1 powder. The AlSi1 particles act as physical barriers in the polymer matrix, increasing the flow resistance and, as a result, the viscosity of the mixture.

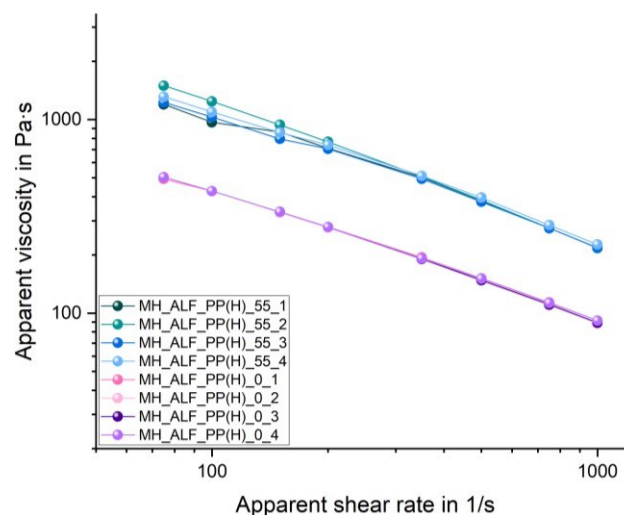


Fig. 14 Cyclohexane debinding formulation, PP(H) apparent viscosity mean curves

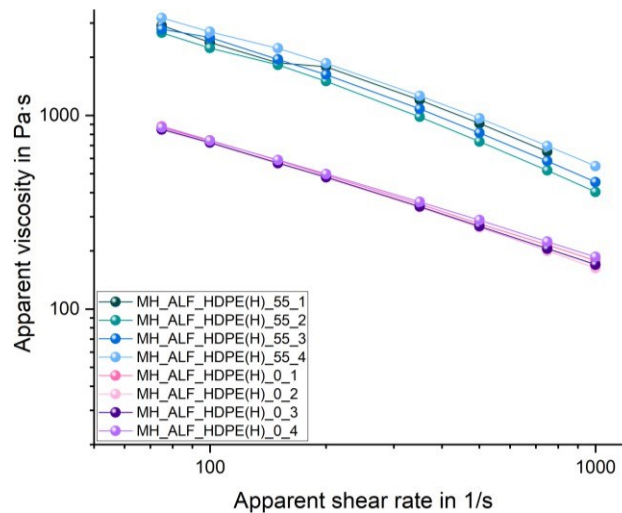


Fig. 15 Cyclohexane debinding formulation, HDPE(H) apparent viscosity mean curves

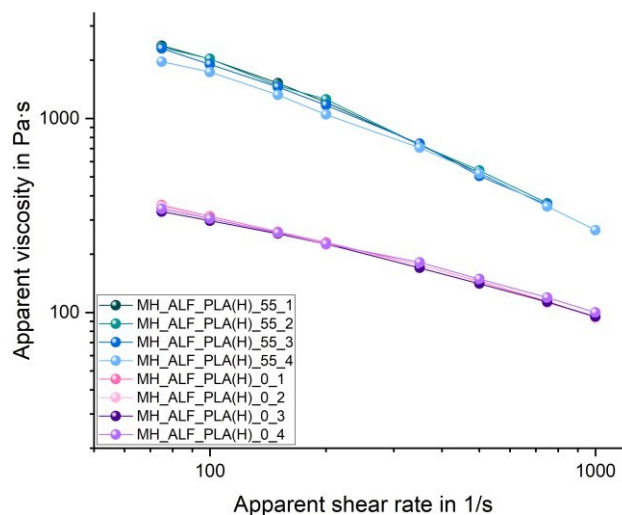


Fig. 16 Cyclohexane debinding formulation PLA(H) apparent viscosity mean curves

When comparing cyclohexane debinding feedstocks, PLA(H)_55, HDPE(H)_55, and PP(H)_55, all formulations using TPE 1 as the main binder, it is noticeable that in the HDPE(H)_55 and PP(H)_55 formulations, viscosity curves increase as the TPE 1 volume percentage decreases, unlike in PLA(H)_55. The increase in viscosity observed in HDPE(H)_55 and PP(H)_55 may be attributed to the chemical composition of PP-MA and HDPE-MA, both of which have been grafted with maleic anhydride, a polar functional group. The presence of this polar group may enhance the connection between the powder and binder system, resulting in a more constrained system due to the increased interaction between the polar groups of the polymer and the AISi1 particles.

In contrast, in PLA(H) feedstock systems, the viscosity curves reduce as the TPE 1 level drops. This implies that the chemical structure of PLA when compared to PP-MA and HDPE-MA

causes less contact between the powder and the binder system. As a result, the system is less restricted and has a lower viscosity when the TPE 1 level is reduced.

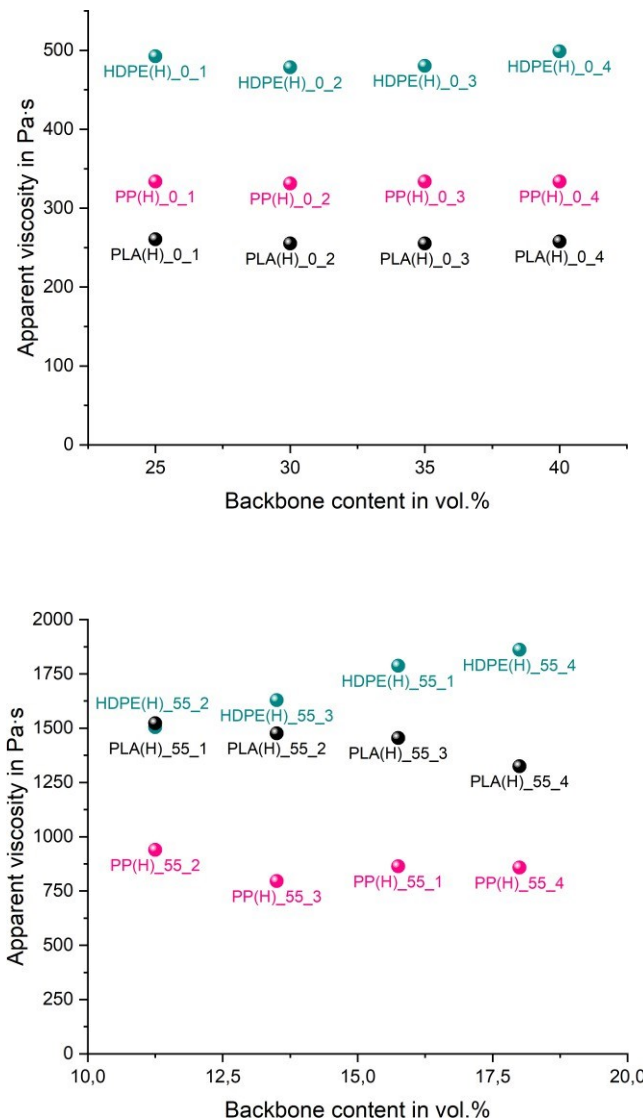


Fig. 17 Comparison of cyclohexane debinding formulations at a shear rate of 150 s^{-1} , top: feedstock systems, bottom: binder systems

Fig. 18 shows that the PP(H)_3 formulations had a lower viscosity than the other three formulations, even though PP(H)_1 and PP(H)_4 have a larger concentration of the backbone component. This observation may suggest the existence of inconsistencies in the powder distribution within the feedstock, which is likely caused by insufficient homogenization during mixing. Deviation in the distribution of powder particles within the binder matrix might result in specific regions having distinct flow characteristics, ultimately causing a reduction or fluctuation in the overall viscosity.

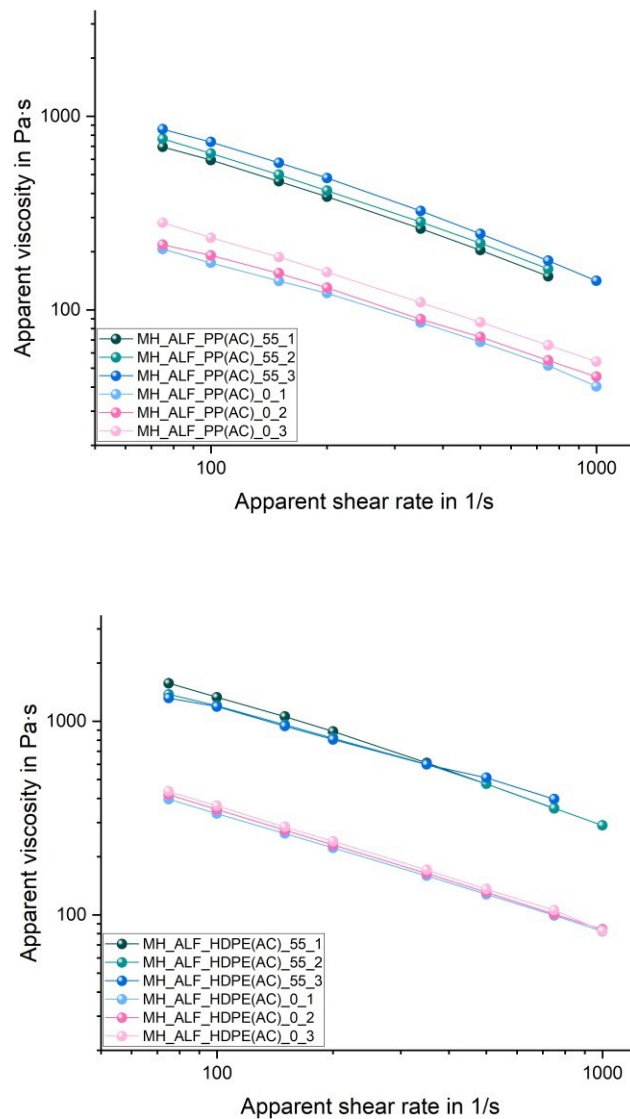


Fig. 18 Acetone debinding formulations, PP(AC) & HDPE(AC), apparent viscosity mean curves

Within the acetone debinding formulations, namely PP(AC) and HDPE(AC), which have a backbone content of 35 vol.%, only the PP(AC) series have a noticeable impact from changes in shore A hardness of TPE 4, the main binder. Significantly, the viscosity of the PP(AC) formulations rises in direct proportion to the Shore A hardness of TPE 4. Out of these options, PP(AC)_3, which includes TPE 4 with a 70 A Shore hardness, has the maximum viscosity. Subsequently, PP(AC)_2 containing TPE 4 with a Shore hardness of 40 A, and ultimately, PP(AC)_1, utilizing TPE 4 with a Shore hardness of 20 A, exhibited the least viscosity.

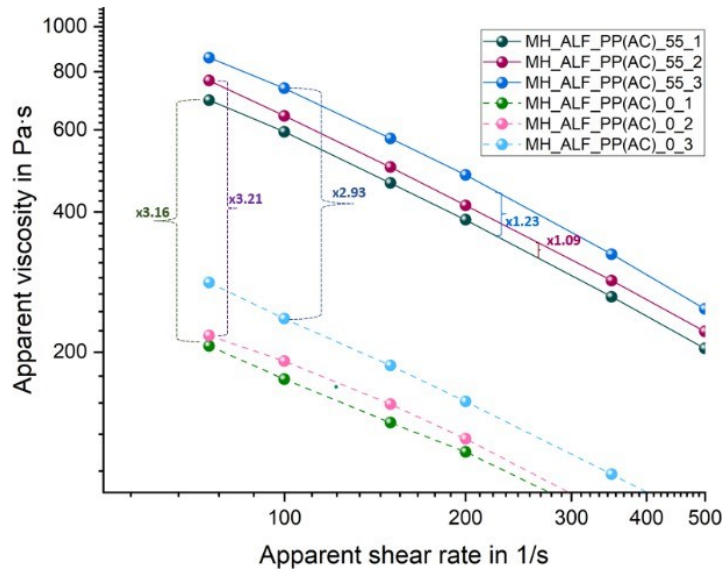


Fig. 19 Overview of the increment in apparent viscosity of PP(AC)

The increment, seen in Fig. 19, in shear viscosity in comparison for the feedstock formulations of PP(AC)_1 is on average 1.23 and 1.09 times for PP(AC)_2 and PP(AC)_3. The observed pattern suggests that the rheological behavior of PP(AC) formulations is greatly influenced by the mechanical properties of TPE 4, particularly its hardness. The correlation between the TPE 4 hardness and the formulation's resistance to flow is indicated by the rise in viscosity as the Shore A hardness increases. Additionally, an increment in shear viscosity, by adding 55 vol.% AISi1 powder in comparison to the binder system is on average 3.16, 3.21, and 2.95 times for PP(AC)_1, PP(AC)_2 and PP(AC)_3.

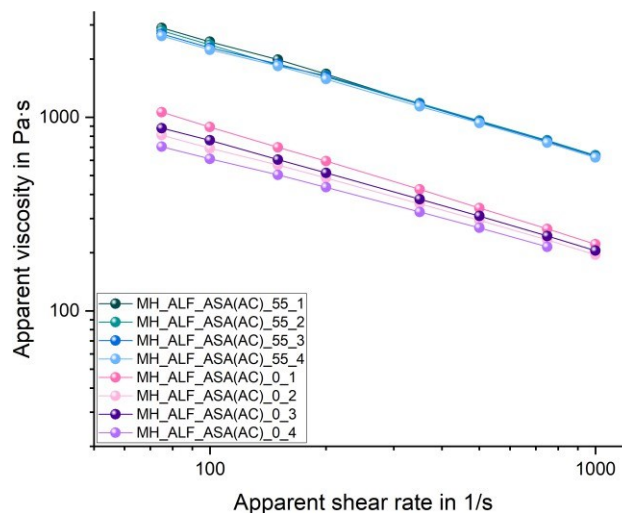


Fig. 20 Acetone based formulations, ASA(AC), apparent viscosity curve

Viscosity curves in acetone debindable formulations using ASA with TSEB as the backbone exhibit variability among different binder compositions. In contrast to other formulations, these formulations do not exhibit a clear and consistent correlation between viscosity and backbone

content. The narrower range of viscosity curves found in the four feedstock samples, in contrast to the wider range exhibited in the viscosity curves of the four binder system samples, can be attributed to the influence of including AlSi1 powder in the feedstock. When AlSi1 powder is added to the feedstock, the physical interactions between the powder and the polymer components (ASA and TSEB) might provide a unifying effect on the viscosity of the material. More precisely, the AlSi1 powder functions both as a filler and as a medium that facilitates a more consistent interaction between the ASA and TSEB components. The powder particles can serve as a bridge, improving the compatibility of the polymers and resulting in a more uniform material system. This can lead to a more uniform viscosity profile across various feedstock compositions. Furthermore, the powder particles also contribute to the increase in viscosity curves.

5.3 Evaluation of the Thermogravimetric Analysis

The thermal degradation of the polymeric binder system is important in the SDS process for sensitive alloys, especially those that include AlSi1. This is because the earliest stages of sintering for aluminum alloys start at temperatures of around 550 °C. The majority of binder polymers undergo degradation when exposed to temperatures near this range. To evaluate the degradation temperatures of the components and the feedstock systems, Thermogravimetric Analysis (TGA) was utilized, and the results are illustrated in Fig. 22-20.

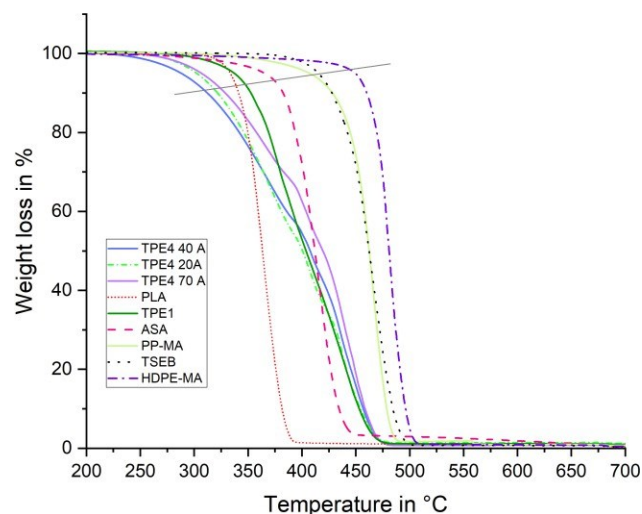


Fig. 21 Representative TGA curve (top sorted following the line from left to right)

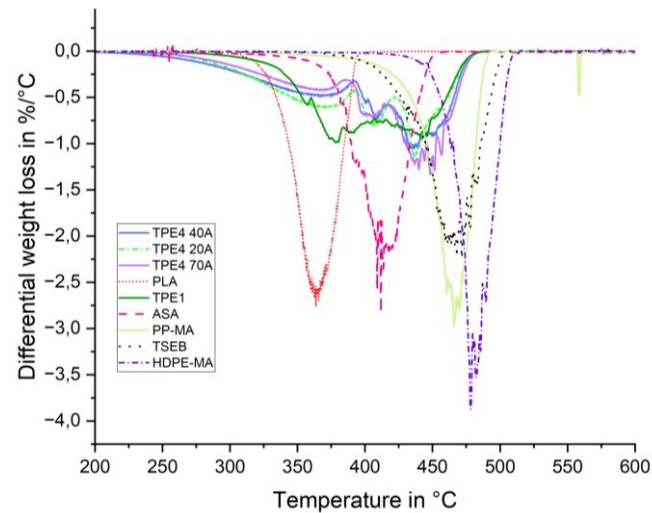


Fig. 22 Representative dTGA curve (bottom) results of backbone and main binder material

The TGA and dTGA revealed comprehensive information about the thermal degradation properties of the backbone and main binder materials, specifically identifying the degradation temperatures T_i and the rates of degradation, see Table 7. The dTGA curves of the backbone exhibited a distinct single peak, suggesting one main degradation mechanism. Notably, HDPE-MA exhibited the highest thermal resistance, with its degradation peak observed at 478 °C. TSEB follows, reaching a peak temperature of 468 °C, and PP-MA reached 466 °C. In contrast, PLA exhibited notably reduced thermal stability, with a degradation temperature of 364 °C. To mention is that the TGA was measured under nitrogen, while the thermal debinding will be done partly in an atmosphere with oxygen and then the degradation will start earlier [19, 24].

The investigation of the remaining mass at a temperature of 500 °C yielded additional information regarding the stability and degradation properties of these polymers. The TSEB exhibited the smallest remaining mass at 0.94 wt.%, suggesting a nearly complete degradation. PLA also had a low residual mass, measured at 1.07 wt.%. However, HDPE-MA exhibited a noticeably greater residue of 4.60 wt.%, indicating that the thermal degradation process was not fully completed, which is confirmed by the final degradation temperature at 512 °C. The elevated residue level in HDPE-MA may pose challenges during the sintering process. The existence of an excessive amount of carbonaceous residues has the potential to impede the quality of sintering, which in turn can have an impact on the mechanical characteristics and structural integrity of the end product.

Table 7 Overview of degradation temperatures of the pure materials

Sample		1 st step		2 nd step		3 rd step		Residue in wt.% at 500 °C
		T _i	T _e	T _i	T _e	T _i	T _e	
		in °C						
Main binder	TPE 4 20 A	370	393	406	423	438	488	1.40
	TPE 4 40 A	372	393	408	417	436	487	0.95
	TPE 4 70 A	369	386	407	416	448	488	0.73
	TPE 1	378	408	442	488	-	-	1.14
	ASA	417	456	-	-	-	-	2.97
Backbone	PP-MA	466	493	-	-	-	-	1.71
	HDPE-MA	478	512	-	-	-	-	4.60
	PLA	364	399	-	-	-	-	1.07
	TSEB	468	506	-	-	-	-	0.94

Comparing the main binders, TPE 4 20 A, TPE 4 40 A, TPE 4 70 A, TPE 1, and ASA, for thermal degradation properties only ASA displayed one main degradation peak at 417 °C, reaching a final degradation temperature of 456 °C. In contrast to TPE 1, this behavior exhibits a degradation process consisting of two distinct steps. The first stage occurs at 378 °C, whereas the second step occurs at 442 °C. This pattern indicates an intricate degradation mechanism that includes various components or phases inside the polymer. Furthermore, every version of TPE 4 exhibited three identifiable degradation peaks. The occurrence of these peaks was consistent across different hardness grades of the material, within a specific temperature range. The initial degradation peak occurred at a temperature of 370 °C, which was then followed by subsequent degradation peaks at 407 °C and 440 °C. The third peak's sharpness is indicative of being the primary degradation mechanism for all three TPE 4. This may be explained by its chemical structure, particularly the different temperatures at which its soft and hard segments degrade.

ASA displayed the largest residual mass of 2.97 wt.%, indicating a lower level of degrading efficiency and prolonged degradation process. Conversely, the TPE 4 series exhibited a relationship where higher shore hardness was associated with lower residue formation. More precisely, TPE 4 70 A, which is the most rigid variant in the series, had the lowest amount of residue at 0.74 wt.%. TPE 4 40 A and TPE 4 20 A, on the other hand, had higher residue levels of 0.95 wt.% and 1.40 wt.%, respectively.

To provide a clearer understanding of how the inclusion of metal particles affects the thermal properties of the binder system, TGA curves were utilized to evaluate the feedstocks. Interestingly, all feedstock systems exhibited a two-phase deterioration curve, mainly because the binder system is made up of two components, each of which has its specific degradation characteristics. This effect, shown in the TGA curves, Fig. 24, was especially visible in the feedstock systems developed for acetone.

The TGA and dTGA curves of PP(AC) and HDPE(AC), which include TPE 4 as the main binder, exhibit notable changes in degradation characteristics when compared to the pure TPE 4 TGA and dTGA curves. Contrary to the usual three-peak degradation pattern seen in pure TPE 4, the TGA and dTGA curves for PP(AC) and HDPE(AC) feedstock display just two primary degradation peaks.

Table 8 Overview of degradation properties of the PP(AC) and HDPE(AC) feedstock

Sample	1 st step		2 nd step		Residue in wt.% at 500 °C	AlSi1 in wt.%	Δ Residue in wt.%
	T _i	T _e	T _i	T _e			
	in °C						
PP(AC)_55_1	344	389	453	491	79.71	78.82	0.89
PP(AC)_55_2	344	393	455	493	80.10	78.96	1.14
PP(AC)_55_3	356	366	458	494	75.45	78.82	-3.37
HDPE(AC)_55_1	353	420	472	508	80.03	78.46	1.57
HDPE(AC)_55_2	335	412	469	508	79.32	78.61	0.71
HDPE(AC)_55_3	353	416	471	510	80.02	78.46	1.56

The thermal degradation profile of HDPE(AC) exhibits a distinct convergence of the second and third peaks of TPE 4 with the primary degradation peak of HDPE. Furthermore, the samples exhibit a considerable decrease in degradation temperatures, as explained in the table. The decrease in temperatures and rates of degradation can be attributed to the addition of AlSi1 particles. The increased thermal conductivity of the material allows for faster heat transport inside the feedstock, which in turn affects its thermal stability and the degradation kinetics. The shift is more pronounced in the first peak, suggesting that the AlSi1 particles are in the TPE 4 phase. Moreover, the intensity of the peaks in the dTGA curves suggests that the main degradation process for these feedstocks mainly takes place at the second peak.

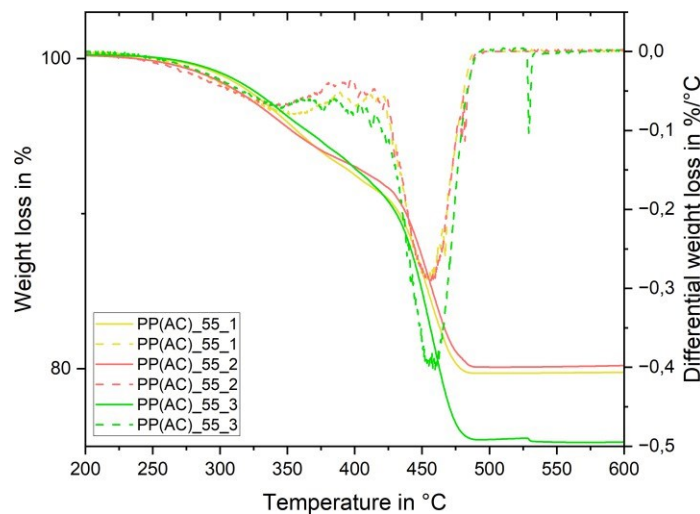


Fig. 23 Acetone debindable feedstock formulations PP(AC) representative TGA and dTGA curves

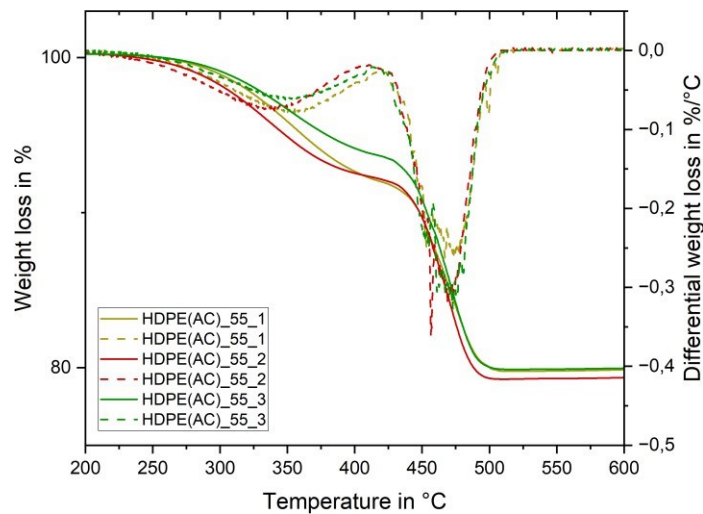


Fig. 24 Acetone debindable feedstock formulations HDPE(AC) representative TGA and dTGA curves

In contrast, the dTGA curve for PP(AC) does not exhibit the distinct overlap observed in HDPE(AC). Conversely, there are small fluctuations ranging from 380 °C to 420 °C, which correlate to comparable degrees of weight reduction. Regarding residue analysis at a temperature of 500 °C, the residues should be the same as the weight percentage of the AlSi powder content, which is 78.7 wt%. For example, the residual percentage for PP(AC)_3 is significantly low at 75.45 wt.%, indicating a possible lack of powder content in the formulation or an uneven distribution of the powder components.

The thermogravimetric measurements of the ASA(AC) feedstock using four different formulations demonstrated a two-step degradation process. This degradation pattern corresponds to the thermal properties seen in the individual binder materials, ASA and TSEB. The first degradation peak for all formulations takes place at around 420 °C, followed by a further degradation peak at around 503 °C, see Table 9.

Table 9 Overview of degradation properties of the ASA(AC) feedstock

Sample	1 st step		2 nd step		Residue in wt.% at 500 °C	AlSi1 in wt.%	Δ Residue in wt.%
	T _i	T _e	T _i	T _e			
	in °C						
ASA(AC)_55_1	420	458	471	501	77.53	76.15	1.38
ASA(AC)_55_2	420	454	473	504	78.17	76.27	1.91
ASA(AC)_55_3	421	454	470	504	77.89	76.40	1.49
ASA(AC)_55_4	420	451	469	503	78.90	76.53	2.37

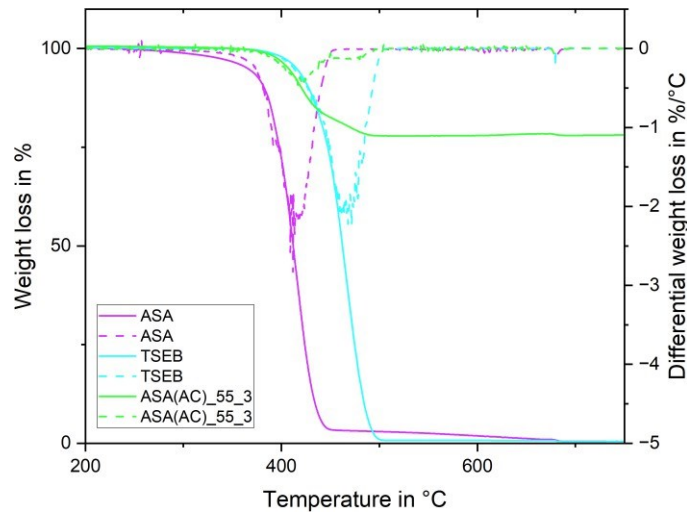


Fig. 25 Acetone debindable feedstock formulations ASA(AC) representative TGA and dTGA curves

However, there was no noticeable pattern seen between the amount of backbone material and changes in degradation temperatures. This suggests that changes in the backbone content of TSEB do not have a substantial impact on the temperatures at which the material degrades. This indicates, that the temperatures at which degradation occurs are mainly determined by the inherent characteristics of the individual components, rather than the proportions in which they are present. Upon analysis of the residual mass at a temperature of 500 °C, it is evident that ASA(AC)_4 displayed the greatest value, measuring 2.37 wt.%. The average residue of the ASA(AC) formulation is around 1.78 wt.%. Additionally, a shift in the TGA curve is observed at 675 °C, similar to the shift shown in the TGA curve of the ASA component. This indicates the existence of remaining ASA components also in the feedstock system, which experience their last stage of degradation at this high temperature. The presence of ASA residues in the feedstock might cause difficulties during the sintering process, which may lead to a worse quality of the final sintered part.

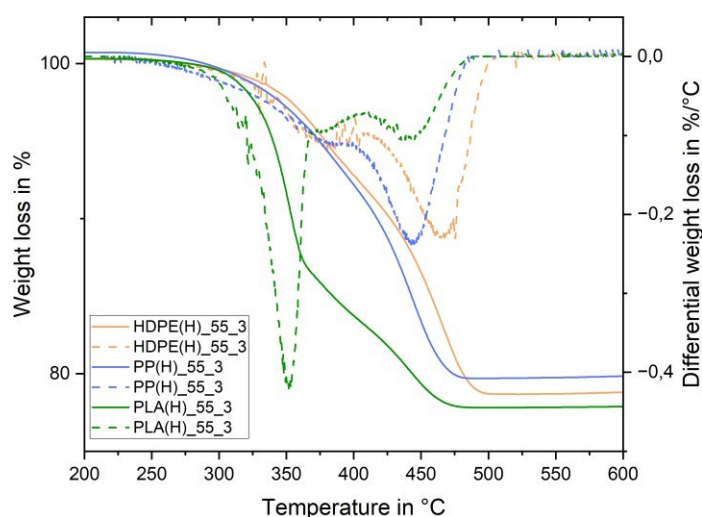
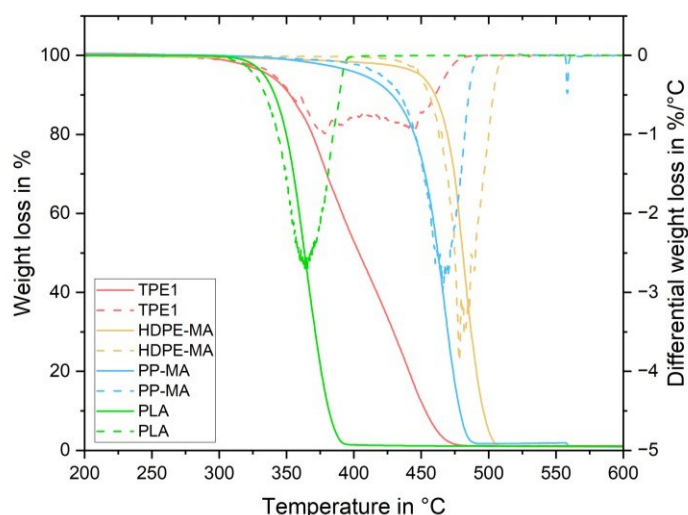


Fig. 26 Cyclohexane debindable binder (left) and feedstock (right) formulations, HDPE(H), PP(H) and PLA(H), representative TGA and dTGA curves

The degradation process of PLA(H) feedstock is 2 step degradation process with the 1st peak at around 353° C. The TGA curves closely mimic the shape of the pure PLA and TPE 1 curve, particularly at 360 °C, where a noticeable change in the slope corresponds to a weight reduction of approximately 10 wt.%. This shift indicates that the backbone component of the PLA(H) is approaching total degradation. The thermal degradation process of the PLA(H) feedstock reaches its final degradation temperature at around 490 °C.

Table 10 Overview of degradation properties of the PLA(H) feedstock

Sample	1 st step		2 nd step		Residue in wt.% at 500 °C	AlSi1 in wt.%	Δ Residue in wt.%
	T _i	T _e	T _i	T _e			
	in °C						
PLA(H)_55_1	350	408	442	490	77.48	76.42	1.06
PLA(H)_55_2	351	408	443	489	78.02	76.16	1.86
PLA(H)_55_3	353	410	440	489	77.81	75.90	1.91
PLA(H)_55_4	356	412	441	491	77.50	75.65	1.85

The HDPE(H) feedstock formulation has a visible dual peak profile, which is affected by the constituent components of the feedstock, TPE 1 and HDPE. Pure TPE 1 shows two degradation peaks, whereas HDPE has just one degradation peak. The dTGA curve shows that the second degradation peak of TPE 1 overlaps with the main degradation peak of HDPE. This interaction leads to a more prominent second peak in the dTGA curve of the HDPE(H) formulation. The degradation of HDPE(H) reaches its completion at a higher final temperature of around 510 °C, indicating its higher thermal stability in comparison to the PLA raw material.

Table 11 Overview of degradation properties of the HDPE(H) feedstock

Sample	1 st step		2 nd step		Residue in wt.% at 500 °C	AlSi1 in wt.%	ΔResidue in wt.%
	T _i	T _e	T _i	T _e			
	in °C						
HDPE(H)_55_1	367	388	469	502	78.44	77.79	0.65
HDPE(H)_55_2	383	401	461	501	79.02	77.80	1.22
HDPE(H)_55_3	381	395	464	505	78.70	77.81	0.89
HDPE(H)_55_4	371	387	469	511	78.85	77.82	1.03

PP(H) feedstock displays thermal degradation properties that are similar to those of the HDPE(H) feedstock. The dTGA curve of the materials shows a degradation temperature of approximately around 386 °C.

Table 12 Overview of degradation properties of the PP(H) feedstock

Sample	1 st step		2 nd step		Residue in wt.% at 500 °C	AlSi1 in wt.%	ΔResidue in wt.%
	T _i	T _e	T _i	T _e			
	in °C						
PP(H)_55_1	380	401	448	489	79.85	78.05	1.80
PP(H)_55_2	391	404	446	489	78.85	78.10	0.75
PP(H)_55_3	386	396	447	490	79.36	78.16	1.20
PP(H)_55_4	388	402	448	491	79.21	78.22	0.99

The thermal degradation temperature of HDPE(H) was determined by TGA experiments conducted in a nitrogen atmosphere, and it was found to be quite elevated. These findings can be better understood by comparing them to the research conducted by Dr.Pöhle [24] on HDPE(H). His research demonstrates how factors like solvent usage, thermal debinding programs, and atmospheric conditions have a significant influence on the thermal degradation properties of polymers.

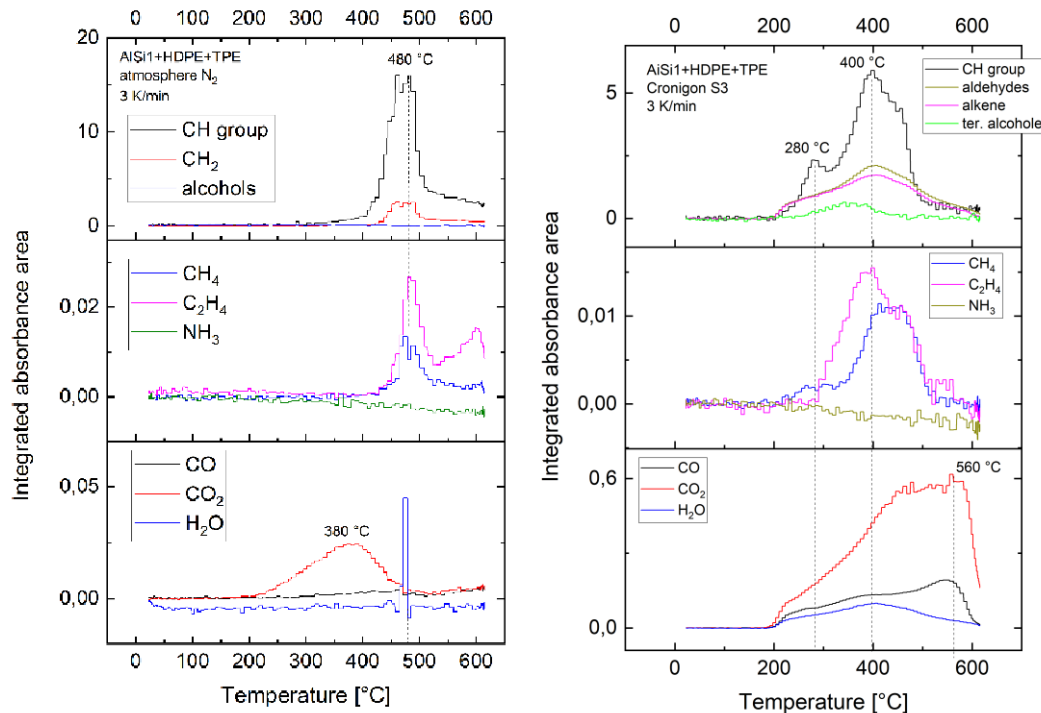


Fig. 27 FTIR process gas analysis of HDPE in Nitrogen (left) and Cronigon S3 (right) atmosphere [24]

The tests utilized Fourier-transform infrared (FTIR) process gas analysis to monitor the thermal debinding process under a nitrogen atmosphere. The heating rate was kept constant at 3 K/min, and the holding temperature was set at 400 °C for 120 min. The primary peak for the CH group signals was determined to be at 480 °C. In addition, a second peak was detected at a temperature of 600 °C when the experiment was conducted in a nitrogen atmosphere. By using Cronigon S3 atmosphere, consisting of Argon and 3 mol% O₂, the peak for the CH group signals is observed at around 400 °C. The occurrence of CH groups, ethylene (C₂H₄), and methane (CH₄) signals, with peaks at 280 °C and 400 °C respectively, is indicative of the degradation of large molecular polymers. The presence of two separate peaks is indicative of the dual-component composition of the binder system employed in these formulations, TPE 1 and HDPE. Significantly, the solvent debinding phase primarily eliminated TPE, as evidenced by the notably reduced intensity of the peak at 280 °C [24].

The differential peak intensity highlights the efficacy of the solvent debinding process in selectively eliminating components of the binder system, which subsequently impacts the thermal stability and decomposition pathway of the residual polymer binder matrix. The differences in thermal degradation profiles observed under different atmospheres indicate that the environmental variables during thermal debinding can modify the kinetics and thermal behavior of polymer degradation [24].

In conclusion, the TGA curves of the feedstock systems indicate that all systems, HDPE(H), PP(H), PLA(H), AS(AC), HDPE(AC) and PP(AC), demonstrate a thermal degradation temperature range that aligns well with the specifications of the AISi1 sintering in the SDS process. The presence of residual ASA components in the feedstock of ASA(AC) is the cause of the exception. These components degrade at a temperature of 675 °C, which may potentially affect the quality of the final parts during sintering. The unique characteristic of the

ASA feedstock may make it less suited for the SDS process for AISi1 due to the potential of low final sintering quality. In contrast, the PLA feedstock has highly favorable qualities for the SDS process, notably its lower final degradation temperature of approximately 490 °C. This characteristic implies that PLA feedstock has the potential to be more compatible with the SDS process, which is likely to lead to better sintering quality and dimensional stability of the finished parts. Other feedstock systems, PP(H), HDPE(H), PP(AC) and HDPE(AC), have a final degradation temperature of approximately 500 °C and are still within an acceptable range for the SDS process. However, they may not offer the same level of efficiency or quality assurance as the PLA feedstock. Additionally can be seen [24], that by employing different thermal debinding atmospheres the degradation temperature can be optimized.

5.4 Evaluation of the DSC Results

Differential scanning calorimetry (DSC) was employed to examine the thermal characteristics and quantify the level of crystallinity. Fig. 29 - Fig. 39 display the thermographs of pure polymers, binder systems, and feedstocks, while Table 13 -18 provide the corresponding thermal properties. The melting temperature is denoted as T_m the crystallization temperature is denoted as T_c and the degree of crystallinity is represented as X_c .

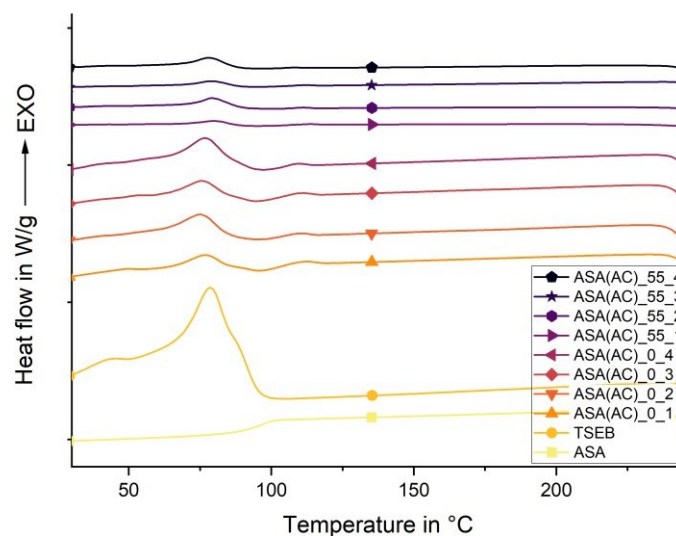


Fig. 28 Representative DSC heating curve of pure materials, binder system and feedstock for ASA formulations in acetone debindable

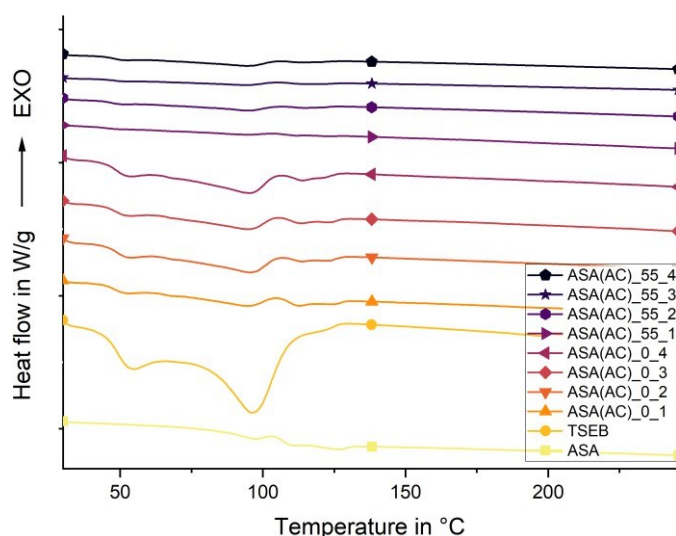


Fig. 29 Representative DSC cooling curve of pure materials, binder system and feedstock for ASA formulations in acetone debindable

The results of ASA(AC) are presented in Table 13 and Fig. 29. The thermograph of ASA reveals a change in the baseline at approximately 108 °C, which is commonly associated with the glass transition temperature (T_g) of the material. In the case of TSEB, there is a clear presence of a dual melting peak at approximately 94 °C. This behavior suggests the existence of two separate crystalline microstructures within TSEB, which is a copolymer of ethylene butyl acrylate copolymer. The binder system ASA(AC) exhibits an intermediate thermal state, demonstrating features that connect those reported in pure ASA and TSEB. An important finding from the analysis is that when the ASA wt.% content increases, the normalized melting enthalpy decreases. The observed pattern indicates that ASA does not act as a nucleating agent, but instead seems to impede the process of crystallization. The limitation on crystallization is important because it suggests that ASA has the potential to affect the formation of the microstructure when the blend is subjected to thermal processing and has an influence on the mechanical properties of the feedstock.

Table 13 DSC Results of pure processed materials, binder system and feedstock for ASA formulations in acetone debindable

Sample	Heating			Cooling	
	T_g in °C	T_m in °C	ΔH_m in J/g	T_c in °C	ΔH_c in J/g
ASA	108.67	-	-	-	-
TSEB	-	94.03	-53.97	78.64	60.13
ASA(AC)_55_1	111.53	-	-	79.55	1.85
ASA(AC)_55_2	111.71	-	-	79.29	4.34
ASA(AC)_55_3	111.00	-	-	79.21	2.27
ASA(AC)_55_4	111.29	-	-	78.26	4.54
ASA(AC)_0_1	109.48	93.38	-6.07	76.57	9.17
ASA(AC)_0_2	111.46	95.39	-11.58	75.21	12.55
ASA(AC)_0_3	111.29	94.36	-9.31	76.62	11.70
ASA(AC)_0_4	110.26	94.16	-13.77	77.01	15.73

However, the crystallinity of TSEB could not be calculated because the necessary data was not available, the melt enthalpy of 100 % crystalline TSEB. Nevertheless, a clear impact on crystallization can be observed when comparing the thermograms of the binder system with those of the feedstock. The inclusion of AISi1 particle significantly impedes crystallization, possibly by serving as physical obstacles to crystal development. Additionally, the introduction of AISi1 particle did not have a noticeable impact on the T_g . The glass transition temperature remains constant at around 111 °C for the binder and feedstock formulations. The observed consistency indicates that the presence of AISi1 particles has a noticeable impact on the crystalline structure and thermal behavior, but it does not have a major effect on the molecular mobility during the glass transition phase.

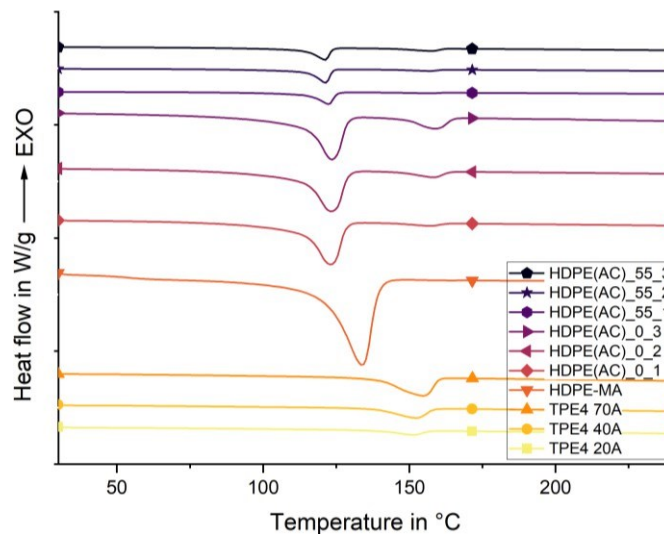


Fig. 30 Representative DSC heating curve of pure materials, binder system and feedstock for HDPE-MA formulations in acetone debindable

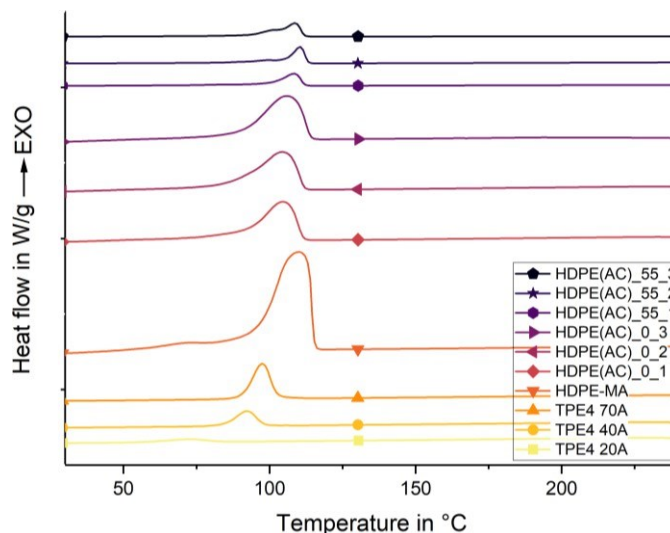


Fig. 31 Representative DSC cooling curve of pure materials, binder system and feedstock for HDPE-MA formulations in acetone debindable

Upon analyzing the melting curves, see Fig. 31, of TPE 4, it was noted that there are clear melting peaks that correspond to different levels of Shore hardness. Specifically, a peak at

151 °C was identified for TPE 4 20 A, 152 °C for TPE 4 40 A, and 154 °C for TPE 4 70 A. The results suggest that the melt temperatures and melt enthalpies grow progressively with the Shore hardness. The observed behavior can be explained by differences in the ratio of soft to hard segments in the microstructure of TPE 4. This supports the notion that a higher Shore hardness is associated with a larger proportion of hard segments.

The HDPE-MA exhibited a melting peak at a temperature of 128 °C, and its crystallinity was determined to be approximately 54.32 %. An observable change in the melting temperature to 123 °C was detected when incorporated with TPE 4 into the binder system. The observed shift indicates that TPE 4 likely functions as a catalyst for nucleation, hence enhancing the crystallization process by shifting the melting temperature to lower temperatures, therefore modifying the composite's melting characteristics. This can also be indicated by the shifts in crystallization temperatures.

Table 14 DSC Results of pure processed materials, binder system and feedstock for HDPE formulations in acetone debindable

Sample	Heating				Cooling		
	T_m^{1st} in °C	ΔH_m^{1st} in J/g	T_m^{2nd} in °C	ΔH_m^{2nd} in J/g	T_c in °C	ΔH_c in J/g	X_c in %
TPE 4 (20 A)	-	-	151.04	-5,63	72.37	4.83	-
TPE 4 (40 A)	-	-	152.11	-13.12	92.39	13.34	-
TPE 4 (70 A)	-	-	154.64	-27.04	97.434	27.71	-
HDPE-MA	128.12	-159.16	-	-	110.19	168.48	54.32
HDPE(AC)_0_1	123.12	-59.75	157.00	-3.05	104.32	65.31	56.44
HDPE(AC)_0_2	123.33	-58.55	158.17	-6.44	104.24	69.89	54.84
HDPE(AC)_0_3	123.49	-60.49	158.86	-12.57	105.92	79.97	57.14
HDPE(AC)_55_1	122.54	-10.45	156.51	-1.18	108.22	12.17	45.84
HDPE(AC)_55_2	121.41	-10.49	156.67	-1.26	110.53	13.59	45.90
HDPE(AC)_55_3	121.05	-9.62	157.29	-2.63	108.55	15.01	42.09

Yet, in the feedstock system, see Table 14, the melting temperature stayed constant at around 122°C, but there was a notable fall in melt and crystallization enthalpy and a considerable drop in crystallinity at an average of 12 %. The significant decrease in crystallinity, in contrast to the binder system's reported crystallinity of around 56%, indicates that the powder component in the feedstock functions as an element that inhibits crystallization. The prevention of crystallization may be attributed to the interference of the powder with the arrangement of polymer chains, thereby hindering the creation of organized crystalline structures.

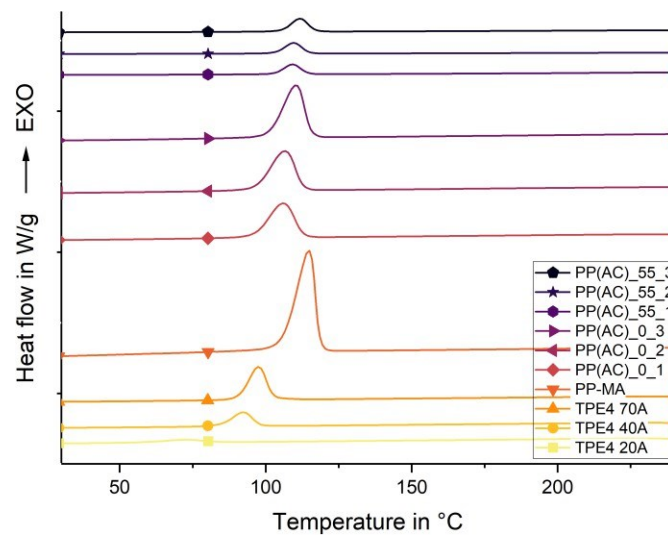


Fig. 32 Representative DSC heating curve of pure materials, binder system and feedstock for PP-MA formulations in acetone debindable

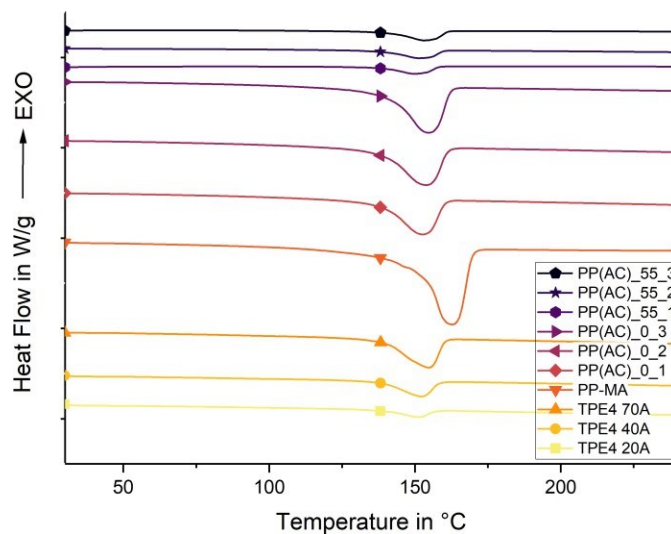


Fig. 33 Representative DSC cooling curve of pure materials, binder system and feedstock for PP-MA formulations in acetone debindable

When comparing the thermogravimetric analysis of PP(AC) to HDPE(AC), it is evident that both materials display similar characteristics in terms of the impact of increased Shore hardness on melting and crystallization enthalpy, as well as crystallinity. Considering the melting temperature ranges of the binder components TPE 4 (about 153 °C) and PP-MA (163 °C) are similar, there is no significant shift in the melting temperature range of the binder system and feedstock formulation, see Table 15. The average melting temperature range is approximately 152 °C. In addition, unlike the HDPE(AC) binder system, the PP(AC) binder system does not exhibit any additional melting peaks. The lack of extra peaks in PP(AC) can

be attributed to the closer alignment of melting temperatures between PP(AC) and TPE 4, which presumably enhances a more synergistic interaction during the melting process.

Table 15 DSC Results of pure processed materials, binder system and feedstock for PP formulations in acetone debindable

Sample	Heating		Cooling		
	T_m in °C	ΔH_m in J/g	T_c in °C	ΔH_c in J/g	X_c in %
TPE 4 (20 A)	151.04	-5.63	72.37	4.83	-
TPE 4 (40 A)	152.11	-13.12	92.39	13.34	-
TPE 4 (70 A)	154.64	-27.04	97.434	27.71	-
PP-MA	162.70	-87.37	114.97	94.28	42.21
PP(AC)_0_1	152.69	-38.99	106.00	39.39	54.15
PP(AC)_0_2	153.69	-44.25	106.70	43.56	60.92
PP(AC)_0_3	154.64	-51.94	110.24	53.07	72.14
PP(AC)_55_1	149.98	-7.59	109.13	7.56	49.75
PP(AC)_55_2	151.41	-8.25	109.58	8.59	54.0
PP(AC)_55_3	153.25	-9.45	111.93	10.13	61.94

Regarding the crystallization behavior, see Table 16, PP(H) binder systems have a crystallization temperature of around 103 °C, compared to T_c of the pure PP-AM around 114 °C. Introducing TPE 1 into the PP(H) binder systems alters the process of crystallization, resulting in a decrease in the temperature at which crystallization occurs. This implies that the PP-MA chains necessitate a larger reduction in energy to properly align with each other and establish a secure crystalline arrangement. The observed behavior suggests that TPE functions as a disruptor during the crystallization process, potentially by generating a heterogeneous nucleating environment or by physically impeding the orderly arrangement of the PP-MA chains.

Table 16 DSC Results of pure processed materials, binder system and feedstock for PP formulations in cyclohexane debindable

Sample	Heating		Cooling		
	T_m in °C	ΔH_m in J/g	T_c in °C	ΔH_c in J/g	X_c in %
TPE 1	75.10	-0.60	-	-	-
PP-MA	162.70	-87.37	114.97	94.28	42.20
PP(H)_0_1	158.09	-29.75	105.47	31.60	60.46
PP(H)_0_2	156.50	-21.11	103.46	19.08	35.68
PP(H)_0_3	157.54	-27.59	104.22	25.08	39.84
PP(H)_0_4	158.57	-35.90	106.20	36.59	45.21
PP(H)_55_1	150.45	-9.17	110.19	9.23	85.02
PP(H)_55_2	150.82	-3.84	111.31	3.69	29.49
PP(H)_55_3	151.49	-5.02	111.69	4.57	33.17
PP(H)_55_4	151.78	-6.84	112.82	7.30	39.52

Furthermore, the addition of AlSi1 particle into the binder systems has a contrary impact, resulting in an elevation of the crystallization temperature to around 111 °C. The increase in AlSi1 particles can be understood as potentially aiding the nucleation process of the polymer. This can occur either by creating sites for nucleation or by modifying the local temperature conditions, resulting in faster and more effective crystallization of the polymer.

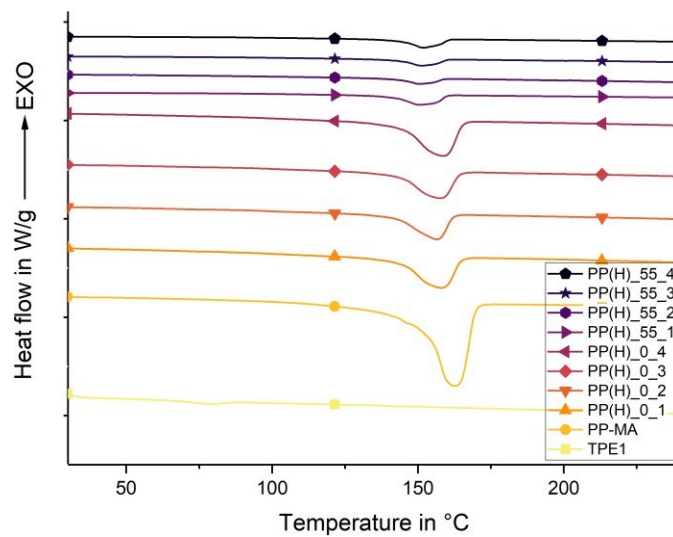


Fig. 34 Representative DSC heating curve of pure materials, binder system and feedstock for PP-MA formulations in acetone debindable

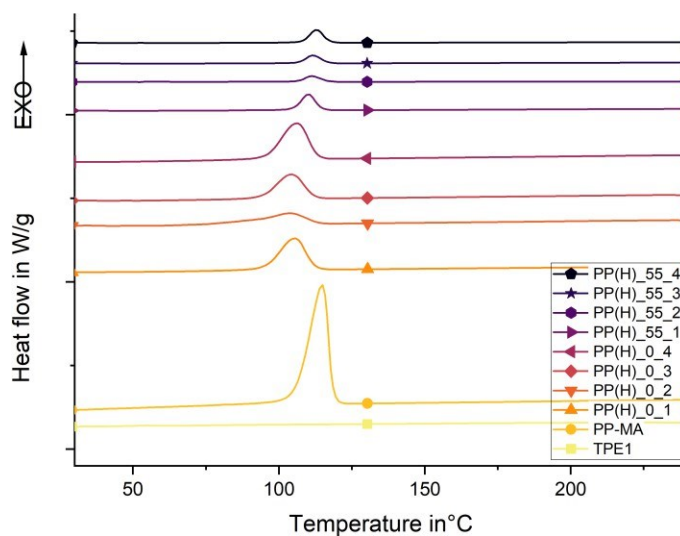


Fig. 35 DSC cooling curve of pure materials, binder system and feedstock for PP formulations in cyclohexane debindable

However, the addition of powder to the binder systems leads to a reduction in the T_m to around 151 °C from T_m around 153 °C. The decrease in mobility of the polymer chains is mostly caused by the presence of metallic particles, which hinders their ability to align and melt evenly. In addition, the inclusion of AISi1 particles in the polymer matrix leads to a decrease in the melting enthalpy.

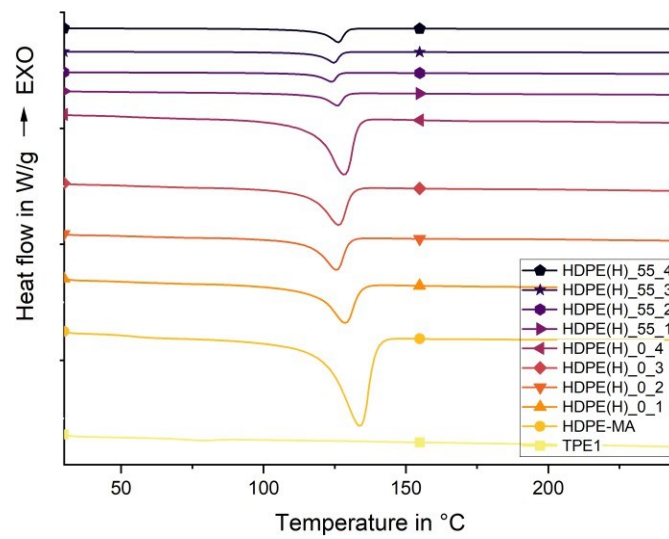


Fig. 36 Representative DSC heating curve of pure materials, binder system and feedstock for HDPE formulations in cyclohexane debindable

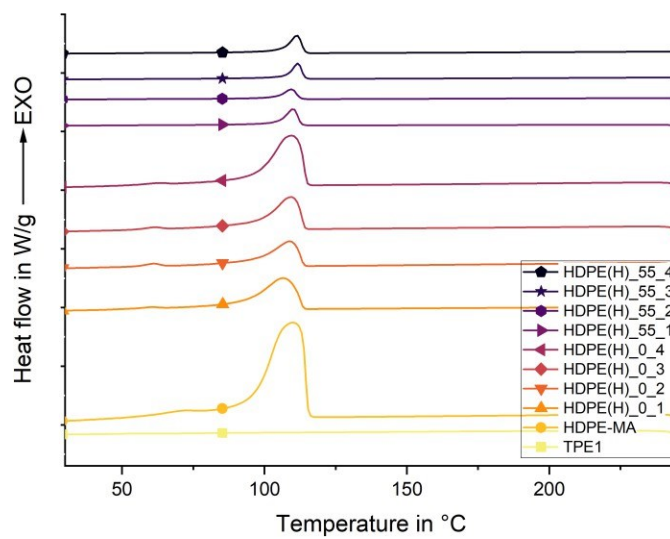


Fig. 37 Representative DSC cooling curve of pure materials, binder system and feedstock for HDPE formulations in cyclohexane debindable

Comparing the values of Table 17 of HDPE(H), similarity to the above-described thermal behaviors from PP(H) is observed.

Table 17 DSC Results of pure processed materials, binder system and feedstock for HDPE formulations in cyclohexane debindable

Sample	Heating		Cooling		
	T _m in °C	ΔH _m in J/g	T _c in °C	ΔH _c in J/g	X _c in %
TPE 1	75.10	-0.60	-	-	-
HDPE-MA	128.12	-159.16	110.19	168.48	54.32
HDPE(H)_0_1	126.86	-53.78	106.44	57.51	73.95
HDPE(H)_0_2	123.78	-40.84	108.97	39.73	46.77
HDPE(H)_0_3	124.47	-48.74	109.30	50.43	47.82
HDPE(H)_0_4	125.70	-79.09	109.53	79.17	67.87
HDPE(H)_55_1	124.54	-10.34	109.90	11.37	64.04
HDPE(H)_55_2	123.96	-6.87	109.40	7.90	35.47
HDPE(H)_55_3	123.37	-9.12	111.96	10.14	40.31
HDPE(H)_55_4	124.99	-13.26	111.37	13.63	51.31

The DSC analysis of pure PLA material shows a distinct change in the baseline at around 62 °C, which corresponds to the glass transition temperature of the PLA phase. The T_g is consistently recorded at approximately 62 °C in all binder systems, and slightly lower at around 60 °C for the feedstock formulations. The result indicates that the flexible sections of the TPE 1 in the binder systems have no significant impact on the glass transition temperature of the PLA phase in the binder system.

Table 18 DSC Results of pure processed materials, binder system and feedstock for PLA formulations in acetone debindable

Sample	Heating					
	T _g in °C	T _m in °C	ΔH _m in J/g	T _c in °C	ΔH _c in J/g	X _c in %
TPE 1	-	75.10	-0.60	-	-	-
PLA	62.20	166.99	-20.55	129.57	29.74	21.87
PLA(H)_0_1	63.03	170.09	-5.87	116.21	5.67	20.57
PLA(H)_0_2	62.32	169.99	-12.25	117.23	13.01	36.29
PLA(H)_0_3	62.91	170.21	-16.76	118.28	16.94	43.17
PLA(H)_0_4	63.16	164.51	-18.87	119.95	19.09	43.13
PLA(H)_55_1	60.82	167.32	-2.24	107.90	1.90	33.29
PLA(H)_55_2	59.78	167.15	-3.69	107.91	3.09	46.19
PLA(H)_55_3	59.44	167.45	-3.36	107.40	2.98	35.89
PLA(H)_55_4	60.06	167.42	-3.93	108.23	3.31	36.88

In contrast to the observed behavior in other formulations such as HDPE(AC), PP(AC), ASA(AC), HDPE(H), and PP(H), PLA samples exhibit a distinct presence of cold crystallization, see Fig. 39 - Fig. 39. More precisely, the cold crystallization temperatures for pure PLA, PLA(H)_0, and PLA(H)_55 are approximately 129 °C, 118 °C, and 107 °C, respectively, as indicated by their respective melting curves. Cold crystallization is a unique occurrence in which the material undergoes crystallization and releases heat when heated to temperatures below its melting point. It demonstrates the capacity of PLA to reorganize its molecular chains and create crystalline structures while being heated, rather than exclusively during the cooling phase.

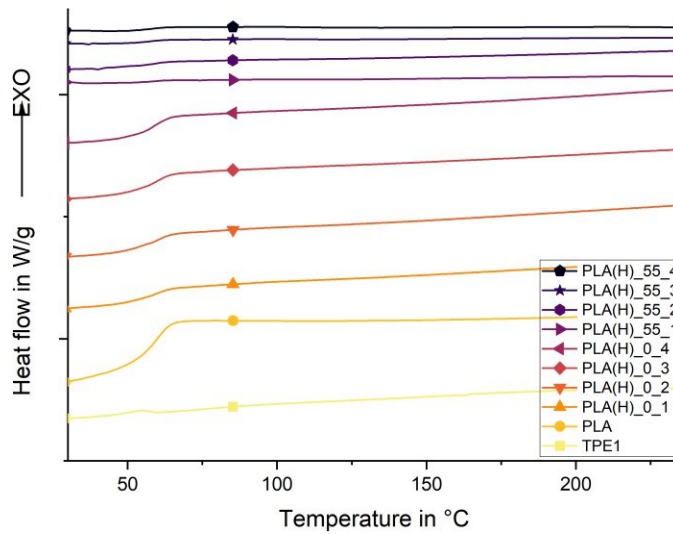


Fig. 38 Representative DSC heating curve of pure materials, binder system and feedstock for PLA formulations in cyclohexane debindable

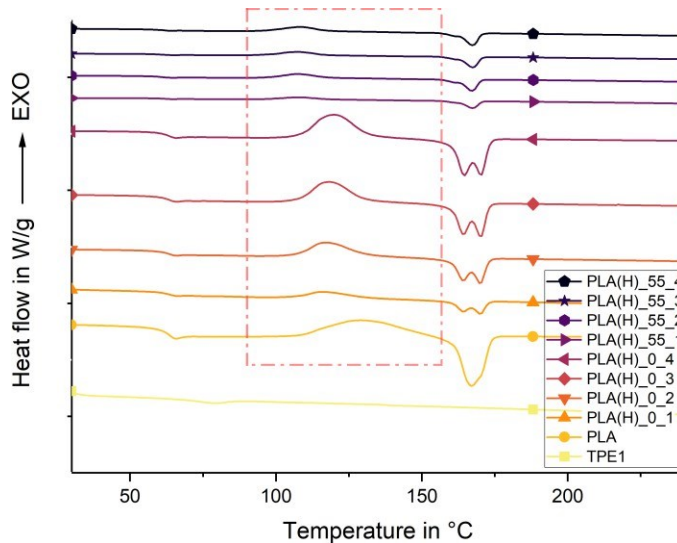


Fig. 39 Representative DSC cooling curve of pure materials, binder system and feedstock for PLA formulations in cyclohexane debindable

Furthermore, there is an observable change in the melting temperature among the different formulations. When compared to the T_m of pure PLA, which is 166 °C, the binder systems show a little increase to 169 °C, while the feedstock has a T_m of 167 °C. Additionally, the observation of a double melting peak in the heating curves of the PLA(H) binder system indicates the presence of two separate crystalline microstructures. The appearance of two distinct peaks suggests the existence of diverse crystalline structures, which could be attributed to changes in cooling rates or the presence of places where nucleation occurs unevenly. Notably, while the soft TPE 1 domain does not function as a nucleating agent to enhance crystallization, it seems to impede the crystallization process. As a result of this limitation, non-uniform PLA

crystals are formed at a lower temperature of around 167 °C. The presence of TPE 1 domains can potentially impact the thermal properties of PLA, leading to changes in its crystallization kinetics and overall thermal stability.

5.5 Evaluation of the Printing Results

Throughout the printing trials, a range of parameters such as printing temperature, bed temperature, nozzle diameter, and layer height were systematically assessed and compared to enhance the 3D printing process for different feedstock formulations. A thorough assessment was essential in determining the optimal parameter combinations that would result in improved print quality for various materials.

Optimal parameter settings were identified for each feedstock formulation. The settings were customized according to the thermal and mechanical qualities of the feedstock, which directly impact the material's behavior during the printing process. The printing temperature was modified to ensure that the material had enough fluidity for extrusion and to promote adequate interlaminar bonding. Similarly, the bed temperature was optimized to improve the adhesion of the initial layer without compromising the structural integrity of the print by making the base excessively soft, which could result in deformities. The nozzle diameter has a significant impact on the resolution and precision of the print. Reduced diameters were discovered to be advantageous in achieving better precision in prints, particularly for elaborate designs, whilst bigger diameters were more suited for expeditious printing and thicker layers. The layer height was a crucial factor that affected the surface quality and printing time. Smaller layer heights often produced smoother surfaces but increased the total printing time. On the other hand, larger layer heights reduced the printing duration, but could negatively impact the surface finish and level of detail. Through the comparison of these characteristics, the most effective combinations were determined for each specific type of feedstock.

Table 19 Overview on the tested printing parameter finding

Feedstock	Nozzle		Temperature		Speed	Layer			
	Diameter	Material	Bed	Printing	in mm/s	Height	Infill		
	in mm		in °C			in mm	in %		
ASA(AC)	0.8	Steel	230	80	10	0.3	100		
	0.6		250	90					
			260	100					
	0.4	Vanadium Carbide	280					0.1	
PP(AC)	0.6	Steel	180	70		10		0.3	100
			220						
			240						
	0.4	Vanadium Carbide	255	90				100	
0.6			Steel	220				80	
	240								
	255	100							
HDPE(AC)	0.6	Steel	220	80	10		0.3	100	
			240						
			255	100					
	0.4	Vanadium Carbide	255	100		0.1			
PP(H)	0.6	Steel	190	80		10	0.3		100
			220						
			240						
	0.4	Vanadium Carbide	255	90			100		
0.6			Steel	220			80		
	240								
	255	100							
HDPE(H)	0.6	Steel	220	80	10		0.3	100	
			240						
			255	100					
	0.4	Vanadium Carbide	255	100		0.1			
PLA	0.6	Steel	180	80		10	0.3		100
			200	90					
			210	100					
	230								
0.4	Vanadium Carbide	230	100	0.1					

The impact of several printing temperatures on the quality of 3D printed parts made from the different formulations was assessed systematically, see Table 19. Some phenomena can be

seen in general, like raising the printing temperatures promoted improved adhesion between the layers of the printed product. The enhancement in interlayer adhesion is crucial as it substantially decreases the occurrence of crack development in the debinded samples.

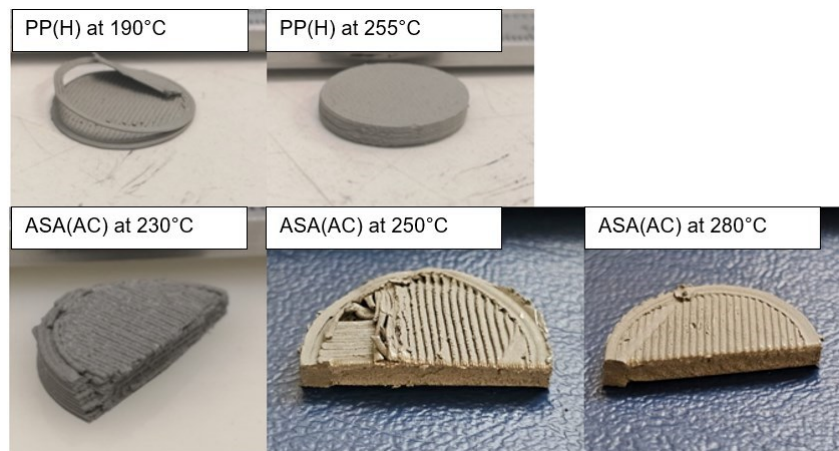


Fig. 40 Influence of temperature on layer bonding on the examples of PP(H) (top) and of ASA (bottom)

In addition, the temperature of the printing bed was gradually increased from 70 °C to 100 °C, while performing experiments to increase the printing temperatures. This modification was essential to avoid the detachment of the initial layer from the printing bed. Debonding frequently arises from the material's contraction during the cooling process, which can cause the material to detach from the bed if the first layer lacks sufficient adhesion. To prevent problems with first-layer adhesion and overall print quality, the issue of material buildup around the nozzle was resolved by changing the nozzle material. This problem is specifically seen in the HDPE(H) formulations, see Fig. 41.

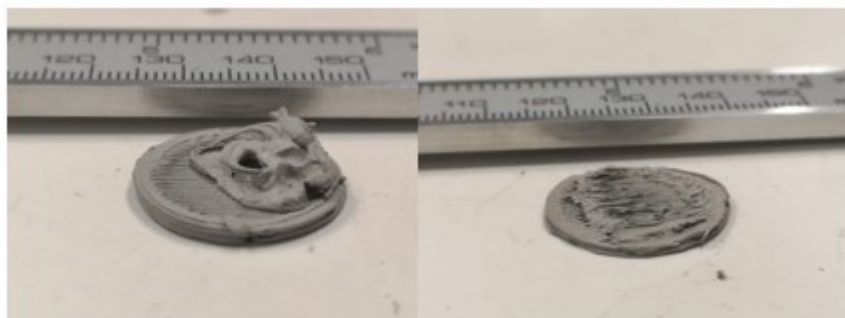


Fig. 41 Debonding due to strong material build-up around the steel nozzle on the example of HDPE(H)

The choice to transition from a conventional steel nozzle to a nozzle composed of vanadium carbide was a successful change. Vanadium carbide nozzles are known for their improved thermal conductivity and decreased friction, resulting in a reduction in material accumulation around the nozzle. This alteration also required a modification in the nozzle diameter to 0.4mm. This smaller diameter allows for a more accurate and regulated extrusion process, resulting in enhanced detail and surface quality in the printed item when compared to larger diameters. Moreover, the decrease in nozzle diameter from 0.8 mm to 0.6 mm in steel variations also had a beneficial impact on the ultimate print quality. Reducing the diameter of the nozzle enables more precise material deposition, resulting in smoother surfaces and more defined details.

This is especially advantageous for elaborate printing where accuracy is essential, such as in complex geometries or situations that need high surface accuracy.

Additionally, occasional clogging of the nozzle and the extruder was observed with all filament formulations. The primary cause of material blockage in the extruder and nozzle was mainly attributed to two problems associated with the filament's properties: softness and irregular diameter. Frequently, these problems resulted in the filament being compressed between the gears of the extruder, leading to blockages and lower printing precision and printability.

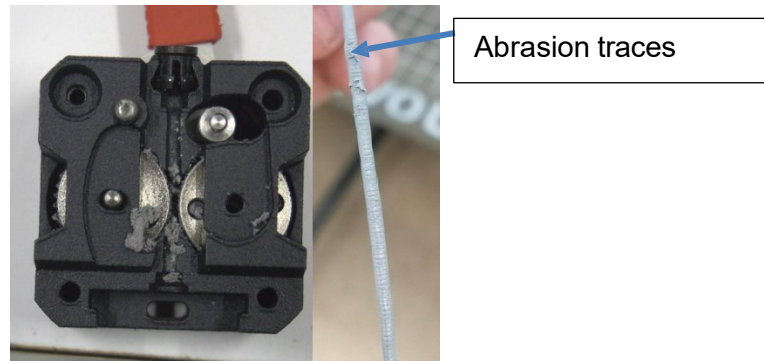


Fig. 42 Material build-up in the extruder between the gear (left) and gear marks on the filament (right)

In response to this issue, the implementation of the LGX shortcut Mosquito Printhead (Bondtech AB, Värnamo, SWE) represented a notable improvement. The used printhead can be described as employing a direct extrusion system. In direct extrusion systems, the filament is introduced directly into the hot end with a short distance between the drive gears and the melting chamber. Comparing the two printhead systems, see Fig. 43, it can be seen that the distance between the drive gears and the melting chamber is reduced. Reducing the length of this pathway aids in preventing excessive compression or deformation of the soft filament before reaching the hot end, hence preserving a consistent force and flow through the nozzle, which is crucial for achieving high-quality extrusion. As a result, it greatly minimizes the chances of filament bending or coiling.

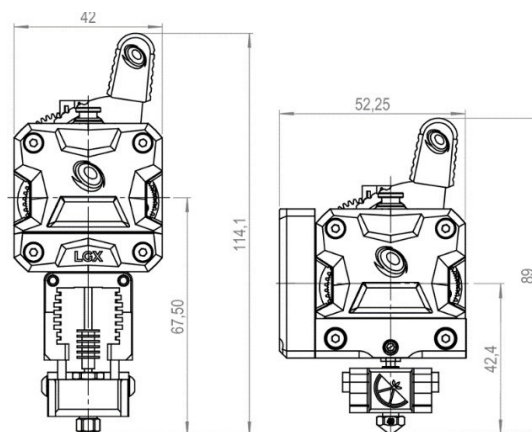


Fig. 43 Comparison of different printheads, LGX with heatbreak (left), right LGX Shortcut Mosquito Printhead [5]

In conclusion, the assessment of print quality using different printing parameters has resulted in the identification of optimal settings for different formulations, see Table 20. A bed

temperature of 100 °C consistently produced the best results in facilitating adhesion between the printing bed and the first layer, while also improving the quality of the initial layers, across all feedstock formulations. Due to the high amount of powder used in these formulations, a printing speed of 10 mm/s was chosen to reduce the occurrence of flaws caused by clogging and uneven layer deposition.

Table 20 Optimized formulations with printing parameters

	Printing temperature in °C	Bed temperature in °C	Printing speed in mm/s	Nozzle diameter in mm
ASA(AC)	280	100	10	0.4
HDPE(AC)	255			
PP(AC)				
PP(H)				
HDPE(H)	230			
PLA(H)				

Additionally, the utilization of a 0.4 mm vanadium carbide nozzle offered benefits because of its minimal adhesive properties with the extruded material. This made extrusion cleaner and decreased the likelihood of uneven material distribution and detachment of the first layer and the print bed while printing. The nozzle material, in conjunction with its smaller diameter, facilitated precise layering at both 0.1 mm and 0.3 mm layer heights, appealing to varying requirements for resolution.

However, different materials exhibited clear preferences when it came to printing temperatures. ASA(AC) demonstrated better interlayer adhesion when printed at a higher temperature of 280 °C. The elevated temperature is believed to enhance the flow and adhesion of the ASA(AC) material, hence minimizing any interlayer problems. Following ASA(AC), HDPE(H), HDPE(AC), PP(H), and PP(AC) exhibited the highest level of adhesion when printed at a temperature of 255 °C. The optimal printing temperature for PLA was determined to be 230 °C. When the temperature drops below this point, there is a clear rise in cracks and delamination while the solvent-debinding process takes place. This negatively affects both the structural strength and appearance of the final part. By setting the temperature to 230 °C, the thermal properties of the PLA are effectively preserved. This ensures that the material holds together properly between layers and maintains its shape during solvent debinding processing step.

5.6 Evaluation of the Debinding Results

5.6.1 Acetone based Debinding

A thorough assessment was carried out to identify the most appropriate backbone, TSEB, TPC, and TPE 3, when combined with ASA. This analysis involved debinding trials and an optical examination of the printed part before and after debinding. The trials used small filament sections and halves of printed discs as samples, which were subjected to debinding in acetone at room temperature for 24 hours. The results of these trials are shown in Fig. 44.

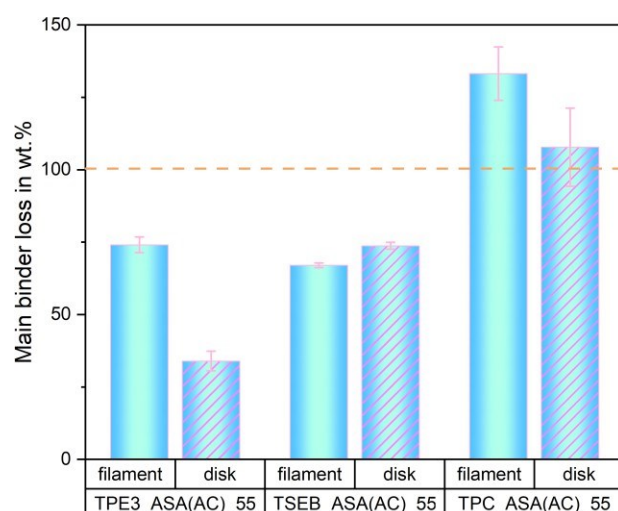


Fig. 44 Debinding results ASA with different backbones

TPC exhibited a significant mass loss, above 100 % for both types of samples, suggesting TPC is not suitable as a main binder for this debinding mechanism. Losses above 100 % mean that some residues stayed in the vessel and contributed to the loss. Images, see Fig. 45, from the optical inspection after debinding show notable swelling and the development of cracks in both the filament and disc samples when TPC was utilized as a backbone. The mechanical integrity of the parts was significantly damaged, resulting in structural failure where the components fragmented and lost their ability to maintain their structural strength during the debinding process.

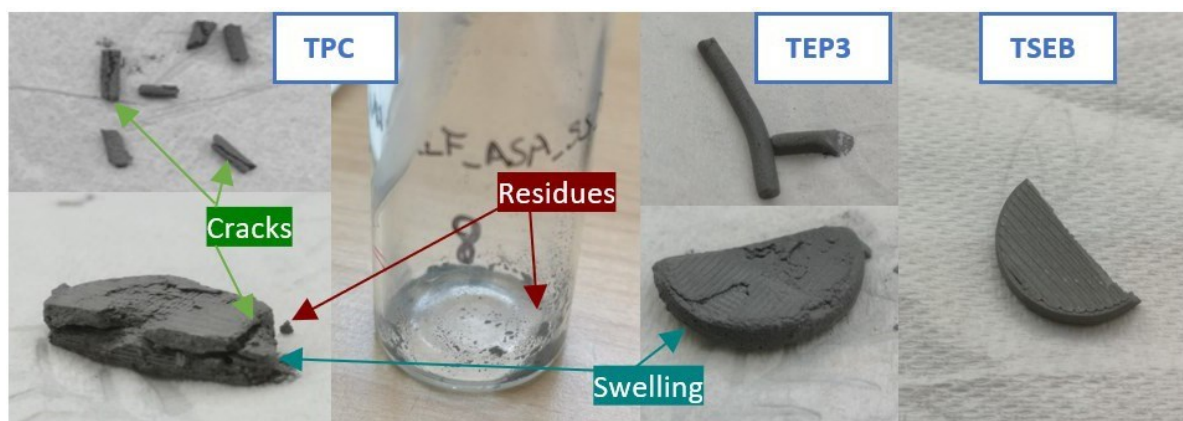


Fig. 45 Optical inspection after debinding of the formulations with different backbones

On the other hand, TPE 3 demonstrated a comparatively small amount of main binder loss, around 33 wt.% for the disc. This indicates a strong interaction between the main binder and the backbone. However, the debinded components displayed significant swelling, indicating possible problems with the efficacy of the debinding process and the compatibility of the materials. TSEB, however, has a main binder weight reduction of around 70 wt.% for both the disc and filament samples. Importantly, after the debinding process, the optical examinations showed no evidence of cracking or swelling, which suggests that both the structural and visual qualities of the pieces were intact.

The data indicate that out of the three backbones examined, TSEB showed the most favorable results in terms of debinding efficiency and the maintenance of part integrity. Therefore, TSEB has been chosen as the backbone material for ASA formulations.

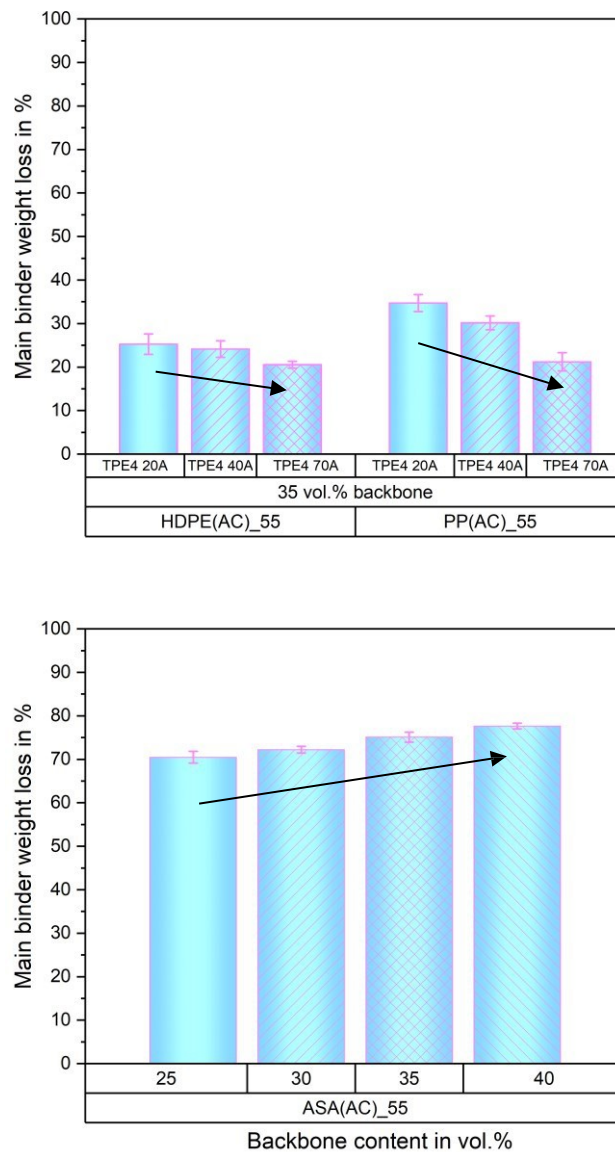


Fig. 46 Debinding results of HDPE(AC), PP(AC) and ASA(AC) in acetone after 24h

When evaluating ASA formulations, see Fig. 44, with different amounts of backbone, and exposing them to acetone for 24 hours, a clear pattern appears that demonstrates the correlation between the volume % of backbone and the effectiveness of debinding. Typically, the debinding rate ranges between 70 % and 75 % in relation to the weight loss of the main binder. The pattern shown indicate that when the volume percentage of the backbone increases, there is a corresponding increase in the weight loss of the main binder. Additional examination of the PP(AC) and HDPE(AC) samples indicate a relatively lower amount of weight loss of the main binder. More precisely, in the case of HDPE(AC), the amount of weight lost falls within the range of 20 to 25 %, while for PP(AC), a slightly higher weight loss of 20 to 35 % is seen in Fig. 44. A consistent pattern is observed in both sample types, indicating a correlation between the weight loss of the main binder and the Shore hardness of the main

binder. It is worth mentioning that a decrease in Shore hardness could be linked to an increase in weight loss. The differences in the chemical structure of the main binder are likely responsible for this observation. The physical qualities, which are governed by the Shore hardness, may affect the interaction with acetone and thus affect the efficacy of the debinding process.

5.6.2 Cyclohexane based Debinding

Fig. 47 shows the performance of PP(H), HDPE(H), and PLA(H) formulations in removing main binders when exposed to cyclohexane for a duration of 24 hours. These formulations, all using TPE 1 as the main binder, exhibit higher percentages of weight loss, suggesting substantial removal of the binder during the debinding process. In contrast to the above results in acetone, which demonstrate a noticeable connection between the amount of backbone or shore hardness and the amount of weight loss of the main binder, these specific results do not indicate a consistent trend among the various formulations.

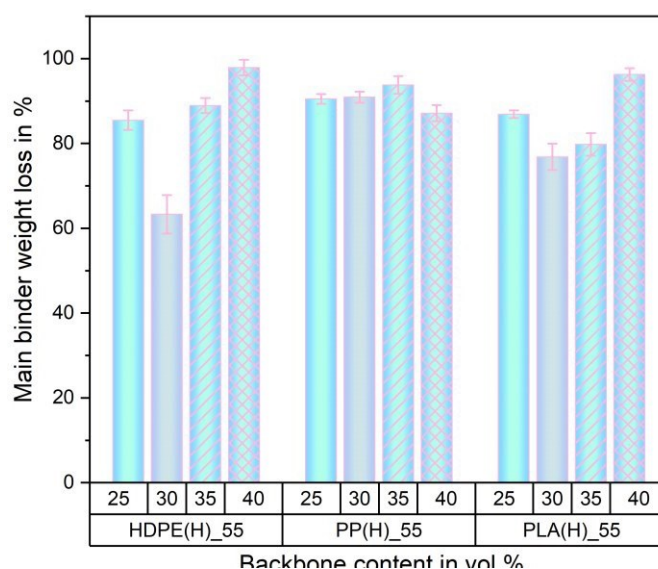


Fig. 47 Debinding results of HDPE(H), PP(H) and PLA(H) in Cyclohexane after 24h

PP(H) formulations provide consistent weight losses across all variations with an approximate 85 % reduction being maintained. The consistent results indicate that when PP(H) is used as the backbone does not affect the debinding of TPE 1 in cyclohexane. This may show that there is an advantageous connection between PP(H) and cyclohexane, which may help in the removal of the main binder.

However, PLA(H) is particularly notable, especially when it contains a backbone concentration of 40 %. In this case, the weight loss reaches up to roughly 96 %, which is the greatest observed. At this particular concentration of backbone, the PLA(H) formulation is extremely susceptible to cyclohexane, resulting in a nearly total loss of the main binder. The high debinding efficiency observed indicates that the chemical compatibility and physical features of PLA at this concentration greatly improve the solvent's capacity to dissolve the main binder.

HDPE(H) formulations exhibit a significant variety in their debinding outcomes. The weight loss varies significantly, peaking at approximately 97 % for a backbone content of 40 % and dropping to roughly 65 % for a 30 % backbone concentration. The significant decrease in

weight loss observed when the backbone content is 30 % suggests that this level may not support an efficient debinding process, potentially due to alterations in the physical structure or chemical interactions within the formulation.

To summarize, all formulations using TPE 1 as the primary binder exhibit excellent debinding efficiency in cyclohexane. However, the degree of binder removal differs greatly depending on the various backbones and their concentrations. PLA(H), specifically with a 40 % backbone content, and HDPE(H) at the same concentration, show the most significant weight losses.

5.6.3 Water based Debinding

The water debinding test performed on pure PVA material exhibited total dissolving within 6 hours at room temperature, showing the water-soluble characteristic of PVA. Nevertheless, when applying water-based debinding test to the feedstock formulations, all samples showed a loss of their structural strength, which was evident from the alteration in the solvent's color. This indicates that the soluble component has dissolved, and parts of the insoluble component remain suspended as particles in the solvent.



Fig. 48 Water debindable test of PVA (left) and PVA/ASA feedstock

These results reveal notable difficulties in creating efficient water-debindable formulations for additive manufacturing applications. The formulations' inability to preserve structural features upon debinding suggests insufficient interaction between the components in watery circumstances. There are multiple reasons for this, such as the ability of the binder components to dissolve in water, the speed at which water spreads throughout the part, or the insufficient bonding or interactions between the material's elements to withstand the effects of the solvent.

Based on the observed full loss of structural integrity, it can be concluded that the debinding trials for water-debindable formulations were unsuccessful. This highlights the need for additional studies and optimization to improve the stability and integrity of these formulations.

5.7 Evaluation of the Contact Angle

Table 21 displays the surface energy values and contact angles with deionized water (θ_w) and diiodomethane (θ_D) for each component of the binder system. The data indicates that a low value in the contact angle with deionized water, a polar liquid, is associated with enhanced wettability. The ability to sufficiently wet a surface allows for a more effective distribution of powder particles throughout the binder system, which is essential for generating homogeneous feedstock materials. Within the components of the binder, HDPE-MA demonstrates the most favorable surface-wetting characteristics, as seen by its notably low contact angle of 45.3°. Next in line comes PP-MA at an angle of 51°, and then PLA at an angle of 57.3°.

Table 21 Overview result of contact angle and surface energy for the binder

Components	Contact angle in °		Surface Energy in mN/m			
	θ_w	θ_D	σ^D	σ^P	σ^T	σ^D/σ^P
PLA	86.6±3.82	57.3±4.07	30.13	3.28	33.41	9.19
HDPE-MA	88.2±4.33	45.3±4.02	36.85	1.66	38.51	22.20
PP-MA	109.1±3.00	51.1±4.96	33.66	0.13	33.79	258.92
TPE 1	101.4±2.43	56.0±3.93	30.87	0.21	31.08	147.00
TPE 4 20 A	114.2±2.19	66.2±3.15	25.02	0.07	25.09	357.43
TPE 4 40 A	111.1±2.77	66.7±4.56	24.73	0.00	24.73	-
TPE 4 70 A	108.4±1.70	64.6±4.41	25.93	0.03	25.95	864.33
ASA	110.0±3.68	62.1±2.82	27.37	0.00	27.37	-
TSEB	86.9±4.68	57.6±1.99	29.96	3.22	33.18	9.30

In addition, the analysis of the surface energy components indicates that PLA exhibits a stronger polar component of 3.28 mN/m, followed by TSEB's polar component of 3.22 mN/m and HDPE-MA's of 1.66 mN/m, in contrast to the main binder components, which have polar components below 0.21 mN/m.

The main binder materials display hydrophobic properties, which are evident in a contact angle exceeding 90° and a significantly reduced polar component. This indicates a low tendency to form bonds with polar substances, which could affect how well they spread and stick to surfaces in contexts where polar substances are dominant.

By analyzing the relationship between the dispersive and polar aspects of surface energy/tension in each phase, one can assess the likelihood of adhesion. In general, the best bonding between two phases occurs when the ratio of these components is roughly aligned, which allows for improved contact at the interface. In this research, none of the backbone and main binder formulations exhibit closely matched values, suggesting possible difficulties in attaining optimal adhesion. However, the two backbone components TSEB with a ratio of 9.30 and PLA with 9.19 would show the required similarity. However, this combination was not able to generate a matching formulation due to their low solubility in the selected solvents, cyclohexane and acetone.

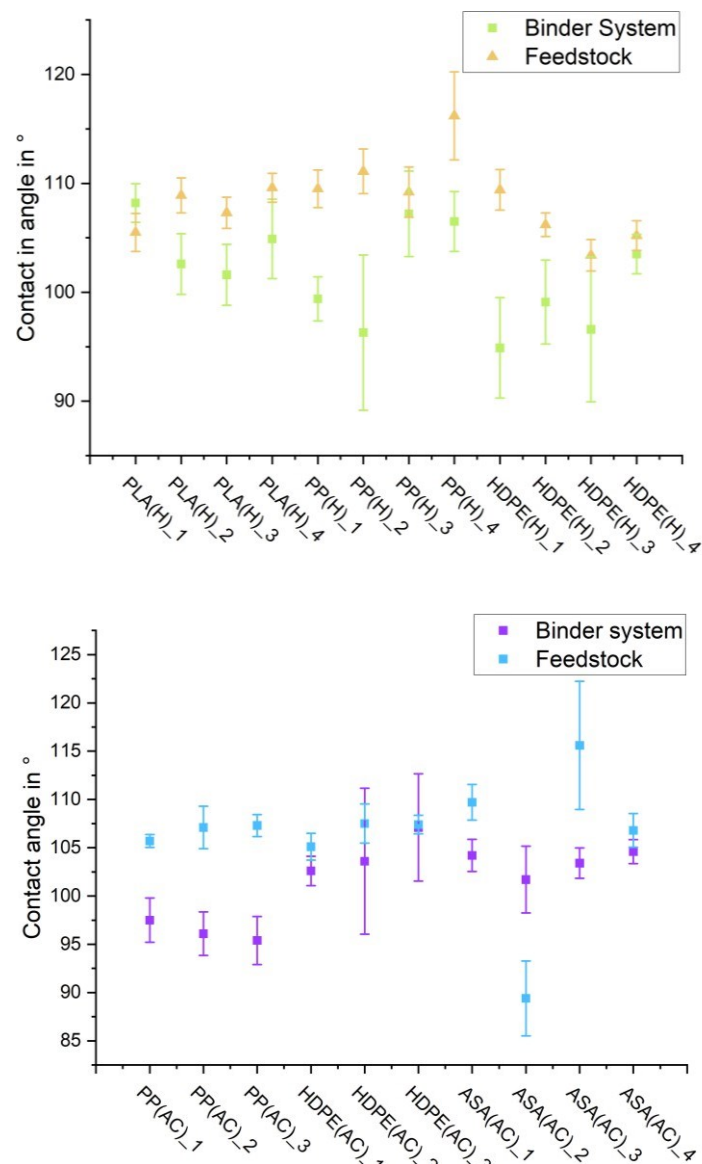


Fig. 49 Comparison of the average contact angle in water for the binder system and feedstock in cyclohexane debindable (left) and in acetone debindable (right)

5.8 Evaluation of the morphological measurements

Scanning electron microscopy (SEM) was employed to analyze feedstock materials of the optimized formulations, HDPE(AC)_55_1, PP(AC)_55_1, HDPE(H)_55_3, PP(H)_55_3, ASA(AC)_55_4 and PLA(H)_55_1. The analyses of the images, Fig. 50, provided a comprehensive characterization of the particle distribution and the incorporation of AISi1 within the samples. In addition, the images allowed for a qualitative assessment of the bond strength between the particles and the polymer matrix, which is essential for comprehending the mechanical characteristics and processing quality of the feedstock.

The SEM image of the HDPE(H)_55_3 sample clearly shows, that the AISi1 particles are not fully covered, and there is a noticeable increase in the agglomeration of particles of different

sizes. The distribution of these particles within the polymer matrix was not uniform, especially in comparison to the PP(H)_55_3 sample. This observation indicates that the insufficient adhesion between the not polar enough HDPE-MA chains and the AISi surface is unable to compensate for the cohesive forces among the AISi1 particles, resulting in their aggregating together. This effect is likely to compromise the structural strength and homogeneity of the composite material.

In contrast, the scanning electron microscope (SEM) images of the PLA(H)_55_1 samples clearly show that the AISi particles have been effectively incorporated into the polymer matrix. This is evident from their well-incorporated structure and even distribution throughout the material. This demonstrates the importance of strong bonding between interfaces, which is crucial for improving the mechanical characteristics of the composite material by guaranteeing a more even distribution of stress when subjected to a load.

The SEM images of the PP(AC)_55_1 and HDPE(AC)_55_1 samples provide additional evidence of strong interfacial adhesion between the particles and the polymer matrix. Furthermore, these samples exhibited no substantial development of AISi1 agglomerates, indicating a consistent dispersion of AISi1 particles inside the matrix.

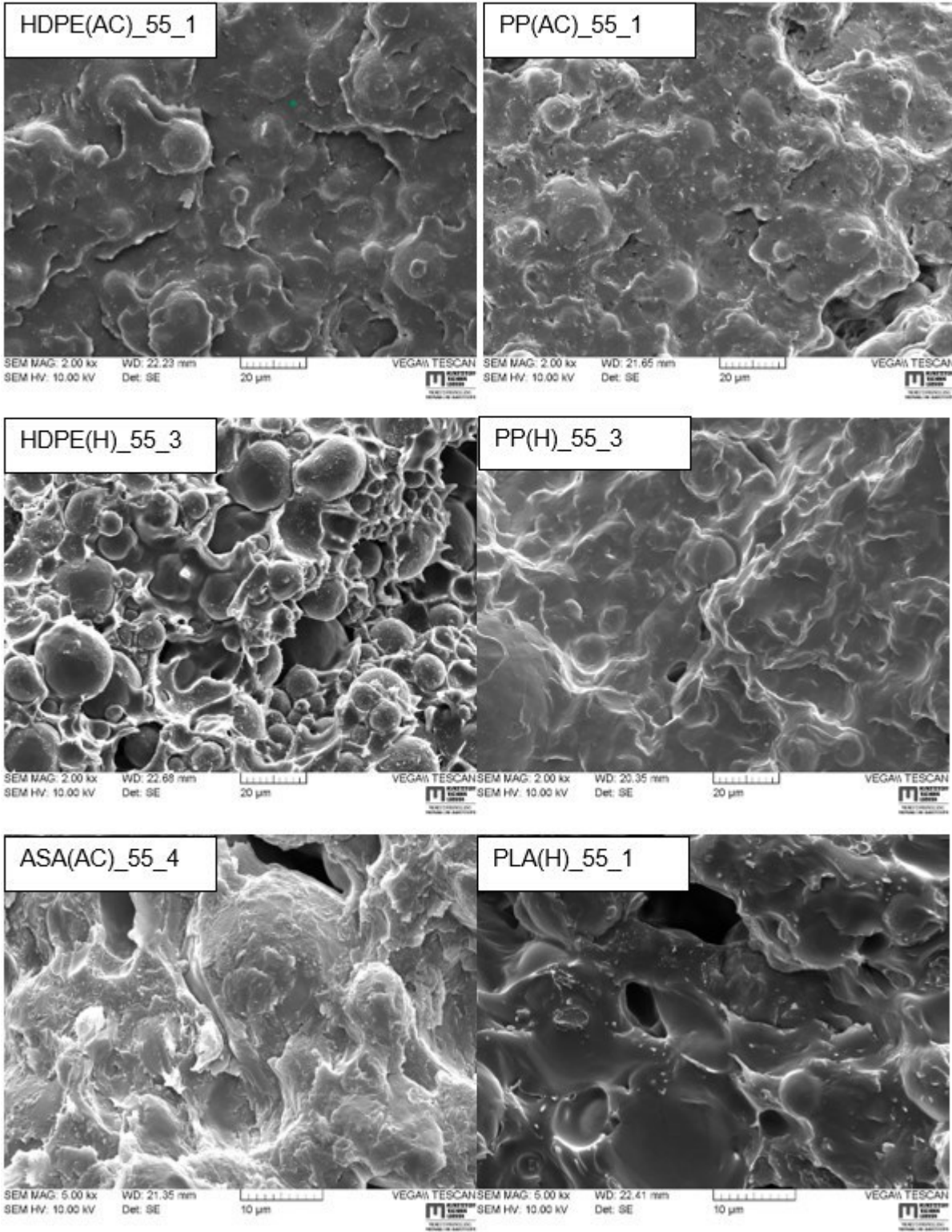


Fig. 50 SEM images in 2k or 5k magnification of the optimized formulations.

6 Conclusion

The primary aim of this Master's thesis was to enhance the comprehension of the AISi1 feedstock, for the MEX processing in the SDS process. To be more precise, the feedstocks for MEX and solvent debinding are being referred to. Therefore, new formulations of binder systems and feedstock were created in a methodical way by assessing the impact of each individual component.

To identify the most effective formulations for each of the six distinct types of binder systems capable of either being debinded by acetone or cyclohexane, the findings of thermal properties (TGA and DSC), rheological characteristics, contact angle, and solvent debinding were compared.

The optimized formulations assessed for acetone debinding are:

- PP(AC)_1 15.75 wt.% PP, 29.25 wt.% TPE 4 20 A, 55 wt.% AISi1
- HDPE(AC)_1 15.75 wt.% HDPE, 29.25 wt.% TPE 4 20 A, 55 wt.% AISi1
- ASA(AC)_4 18.00 wt.% TSEB, 27.00 wt.% ASA, 55 wt.% AISi1

The selection process for the suitable TPE 4 type for each backbone, namely PP-MA and HDPE-MA, exhibited a noteworthy pattern in the debinding results. A clear association between the shore hardness A of TPE 4 and the maximal binder weight loss was revealed through the comparative examination of the debinding data. More precisely, the formulations that included TPE 4 with a shore hardness of 20 A, specifically HDPE(AC)_55_1 and PP(AC)_55_1, showed the most favorable results in terms of debinding efficiency. Therefore, these formulations were regarded as superior in their respective areas.

Regarding ASA(AC), an examination of the debinding process unveiled a distinct pattern in which a rise in the concentration of the TSEB backbone resulted in a corresponding increase in the maximum weight loss. As a result, the formulation ASA(AC)_55_4, which contains a larger amount of TSEB, was determined to be the most effective in obtaining the desired debinding characteristics.

The optimized formulations assessed for cyclohexane debinding are:

- PP(H)_3 15.75 wt.% PP, 29.25 wt.% TPE 1, 55 wt.% AISi1
- HDPE(H)_3 15.75 wt.% PP, 29.25 wt.% TPE 1, 55 wt.% AISi1
- PLA(H)_1 11.25 wt.% PLA, 33.75 wt.% TPE 1, 55 wt.% AISi1

The PP(H)_3 formulation was chosen as the most ideal option for the PP(H) category principally because it demonstrated greater performance in attaining the largest weight loss throughout the debinding process in cyclohexane. This attribute is a clear indication of effective debinding, which is crucial for guaranteeing the integrity and excellence of the end product. Furthermore, PP(H)_3 was preferred since it exhibited a reduced level of crystallization. The decreased crystallinity greatly improves the capacity to wind and process the filament. Decreased crystallinity in the polymer structure often results in enhanced ductility, which is beneficial for lowering the fragility of the filament during the 3D printing process.

The PLA(H)_1 and HDPE(H)_3 formulations are characterized by exhibiting the smallest residue quantities, as indicated by their respective thermogravimetric analysis (TGA) and differential thermogravimetric analysis (dTGA) curves. The presence of low residue levels indicates successful debinding, which is essential for achieving high-quality sintering

procedures. Residual material can have a negative impact on the structural integrity and mechanical qualities of the final product. Furthermore, PLA(H)_1 and HDPE(H)_3 exhibit significant weight reduction during the debinding process, indicating effective removal of the binder components, in addition to their low residue properties.

In addition, HDPE(H)_3 stands out due to its reduced viscosity when subjected to a shear rate of 150 1/s, in comparison to other HDPE(H) compositions. The reduced viscosity of the material allows for better flow properties during the extrusion process, resulting in easier processing and higher quality filament during 3D printing.

In conclusion, the evaluated formulations show significant promise for the use in shaping debinding and sintering (SDS) of AlSi1. Although the early findings on the debinding process and material handling properties are promising, it is crucial to do further research on the sintering behavior of AlSi1 particles in these binder systems. Comprehending the complete influence of each binder system on the sintering process is essential, as this phase is critical in establishing the mechanical characteristics and structural integrity of the end products. An in-depth examination of the impact of AlSi1 particles on the compaction, enlargement of grains, and changes in microstructure during the sintering process will offer valuable knowledge for enhancing the overall efficiency of the SDS process.

7 Literature

- [1] ISO/ASTM 52900: Additive manufacturing - General principles - Fundamentals and vocabulary, 2021-11
- [2] Al-Qudsi, A.; Kammler, M.; Bouguecha, A.; Bonk, C.; Behrens, B.-A.: Comparison between different numerical models of densification during solid-state sintering of pure aluminium powder, *Production Engineering* 9 (1), 2015, pp. 11–24
- [3] Anderegg, D.A.; Bryant, H.A.; Ruffin, D.C.; Skrip, S.M.; Fallon, J.J.; Gilmer, E.L.; Bortner, M.J.: In-situ monitoring of polymer flow temperature and pressure in extrusion based additive manufacturing, *Additive Manufacturing* 26, 2019, pp. 76–83
- [4] Blaine, R.L.: *Polymer Heats of Fusion*
- [5] Bondtech AB: LGX-DD-FF-setups-Technical-Drawings, 2024, [https://3d.nice-cdn.com/upload/file/LGX-DD-FF-setups-Technical-Drawings\[0\].pdf](https://3d.nice-cdn.com/upload/file/LGX-DD-FF-setups-Technical-Drawings[0].pdf)
- [6] Bonten, C.: *Kunststofftechnik, Einführung und Grundlagen*, Hanser, München, 2014
- [7] Bulger, M.: *Powder Injection Molding Tutorial*, International Conference on Injection Molding of Metals, Ceramics and Carbides, 2024
- [8] Galantucci, L.M.; Pellegrini, A.; Guerra, M.G.; Lavecchia, F.: 3D Printing of parts using metal extrusion: an overview of shaping debinding and sintering technology, *Advanced Technologies & Materials* 47 (1), 2022, pp. 25–32
- [9] Gebhardt, A.: *Additive Fertigungsverfahren, Additive Manufacturing und 3D-Drucken für Prototyping - Tooling - Produktion*, Hanser eLibrary, 5. Ed., Hanser, München, 2016
- [10] Gebhardt, A.; Kessler, J.; Thurn, L.: *3D Printing, Understanding Additive Manufacturing*, 2. Ed., Hanser Publications, Cincinnati, Ohio, 2018
- [11] Gibson, I.; Rosen, D.; Stucker, B.: *Vat Photopolymerization Processes*, In: Gibson I.; Rosen D.; Stucker B. (Hrsg.): *Additive Manufacturing Technologies*, Springer New York, New York, NY, 2015, pp. 63–106
- [12] Godec, D.; Gonzalez-Gutierrez, J.; Nordin, A.; Pei, E.; Ureña Alcázar, J.: *A Guide to Additive Manufacturing*, Springer International Publishing, Cham, 2022
- [13] Gonzalez-Gutierrez, J.; Cano, S.; Schuschnigg, S.; Kukla, C.; Sapkota, J.; Holzer, C.: *Additive Manufacturing of Metallic and Ceramic Components by the Material Extrusion of Highly-Filled Polymers: A Review and Future Perspectives*, *Materials (Basel, Switzerland)* 11 (5), 2018
- [14] Gonzalez-Gutierrez, J.; Beulke, G.; Emri, I.: *Powder Injection Molding of Metal and Ceramic Parts*, In: Wang J. (Hrsg.): *Some Critical Issues for Injection Molding*, InTech, 2012
- [15] Hayat, M.D.; Zhang, H.; Karumbaiah, K.M.; Singh, H.; Xu, Y.; Zou, L.; Qu, X.; Ray, S.; Cao, P.: A novel PEG/PMMA based binder composition for void-free metal injection moulding of Ti components, *Powder Technology* 382, 2021, pp. 431–440
- [16] Heaney, D.F.: *Handbook of metal injection molding*, Woodhead Publishing series in metals and surface engineering, WP Woodhead Publishing, Duxford, 2019
- [17] Kaelble, D.H.: Dispersion-Polar Surface Tension Properties of Organic Solids, *The Journal of Adhesion* 2 (2), 1970, pp. 66–81
- [18] Kan, X.; Yang, D.; Zhao, Z.; Sun, J.: 316L FFF binder development and debinding optimization, *Materials Research Express* 8 (11), 2021, pp. 116515
- [19] Menczel, J.D.; Prime, R.B.: *Thermal Analysis of Polymers*, Wiley, 2009

- [20] Mofokeng, J.P.; Luyt, A.S.; Tábi, T.; Kovács, J.: Comparison of injection moulded, natural fibre-reinforced composites with PP and PLA as matrices, *Journal of Thermoplastic Composite Materials* 25 (8), 2012, pp. 927–948
- [21] Momeni, V.; Hufnagl, M.; Shahroodi, Z.; Gonzalez-Gutierrez, J.; Schuschnigg, S.; Kukla, C.; Holzer, C.: Research Progress on Low-Pressure Powder Injection Molding, *Materials (Basel, Switzerland)* 16 (1), 2022
- [22] Momeni, V.; Shahroodi, Z.; Hufnagl, M.; Gonzalez-Gutierrez, J.; Duretek, I.; Schuschnigg, S.; C. Kukla and C. Holzer: Selecting the Suitable Thermoplastic Elastomer as the Main Component in the Feedstock for Metal Material Extrusion of Aluminium, 2024
- [23] Owens, D.K.; Wendt, R.C.: Estimation of the surface free energy of polymers, *Journal of Applied Polymer Science* 13 (8), 1969, pp. 1741–1747
- [24] Poehle, G.; Quadbeck, P.; Riecker, S.; Kukla, C.; Momeni, V.; Schuschnigg, S.: Debinding and sintering strategies for Fused Filament Fabrication (FFF) of aluminium alloys
- [25] Schubert, T.; Pieczonka, T.; Baunack, S.; Kieback, B.: The Influence of the Atmosphere and Impurities on the Sintering Behaviour of Aluminium, 2005
- [26] Sing, S.L.; Tey, C.F.; Tan, J.; Huang, S.; Yeong, W.Y.: 3D printing of metals in rapid prototyping of biomaterials: Techniques in additive manufacturing, In: *Rapid Prototyping of Biomaterials*, Elsevier, 2020, pp. 17–40
- [27] Singh, P.; Balla, V.K.; Tofangchi, A.; Atre, S.V.; Kate, K.H.: Printability studies of Ti-6Al-4V by metal fused filament fabrication (MF3), *International Journal of Refractory Metals and Hard Materials* 91, 2020, pp. 105249
- [28] Suwanpreecha, C.; Manonukul, A.: A Review on Material Extrusion Additive Manufacturing of Metal and How It Compares with Metal Injection Moulding, *Metals* 12 (3), 2022, pp. 429
- [29] Thompson, Y.; Gonzalez-Gutierrez, J.; Kukla, C.; Felfer, P.: Fused filament fabrication, debinding and sintering as a low cost additive manufacturing method of 316L stainless steel, *Additive Manufacturing* 30, 2019, pp. 100861
- [30] Todd, I.; Sidambe, A.T.: Developments in metal injection moulding (MIM), In: *Advances in Powder Metallurgy*, Elsevier, 2013, pp. 109–146
- [31] Tsuji, H.; Horii, F.; Nakagawa, M.; Ikada, Y.; Odani, H.; Kitamaru, R.: Stereocomplex formation between enantiomeric poly(lactic acid)s. 7. Phase structure of the stereocomplex crystallized from a dilute acetonitrile solution as studied by high-resolution solid-state carbon-13 NMR spectroscopy, *Macromolecules* 25 (16), 1992, pp. 4114–4118
- [32] Wang, J.; Xie, H.; Weng, Z.; Senthil, T.; Wu, L.: A novel approach to improve mechanical properties of parts fabricated by fused deposition modeling, *Materials & Design* 105, 2016, pp. 152–159
- [33] Yang, J.; Yang, Y.; He, Z.; Chen, B.; Liu, J.: A Personal Desktop Liquid-Metal Printer as a Pervasive Electronics Manufacturing Tool for Society in the Near Future, *Engineering* 1 (4), 2015, pp. 506–512

8 List of Figures

Fig. 1	Process chain of additive manufacturing [9]	10
Fig. 2	Types of extruder used in MEX. Plunger-based (left), filament-based (middle), screw-based (right) [12]	11
Fig. 3	Overview of processing steps SDS [21]	12
Fig. 4	Binder content during the SDS process steps [12]	14
Fig. 5	Sintering of three particles, showing possible paths of the atomic motion involved with neck growth and densification [6]	16
Fig. 6	Process steps of the SDS process with an overview of which aspects were investigated and which information could be gained	19
Fig. 7	Overview binder and feedstock formulations	20
Fig. 8	Contact angle formation on a solid according to Young [33]	27
Fig. 9	Sample geometry for printing trials [22]	28
Fig. 10	Overview torque measurement HDPE(H)_55	29
Fig. 11	Overview torque measurement curves PP(H)_55 (top), PP(H)_0 (bottom)	30
Fig. 12	Overview torque measurement curves HDPE(AC)_55 (top), PP(AC)_55 (bottom)	31
Fig. 13	Overview torque measurement curves PLA(H)_55 (top), ASA(AC)_55 (bottom)	32
Fig. 14	Cyclohexane debinding formulation, PP(H) apparent viscosity mean curves	33
Fig. 15	Cyclohexane debinding formulation, HDPE(H) apparent viscosity mean curves	34
Fig. 16	Cyclohexane debinding formulation PLA(H) apparent viscosity mean curves	34
Fig. 17	Comparison of cyclohexane debinding formulations at a shear rate of 150 s^{-1} , top: feedstock systems, bottom: binder systems	35
Fig. 18	Acetone debinding formulations, PP(AC) & HDPE(AC), apparent viscosity mean curves	36
Fig. 19	Overview of the increment in apparent viscosity of PP(AC)	37
Fig. 20	Acetone based formulations, ASA(AC), apparent viscosity curve	37
Fig. 21	Representative TGA curve (top sorted following the line from left to right)	38
Fig. 22	Representative dTGA curve (bottom) results of backbone and main binder material	39
Fig. 23	Acetone debindable feedstock formulations PP(AC) representative TGA and dTGA curves	41
Fig. 24	Acetone debindable feedstock formulations HDPE(AC) representative TGA and dTGA curves	42
Fig. 25	Acetone debindable feedstock formulations ASA(AC) representative TGA and dTGA curves	43

Fig. 26 Cyclohexane debindable binder (left) and feedstock (right) formulations, HDPE(H), PP(H) and PLA(H), representative TGA and dTGA curves	44
Fig. 27 FTIR process gas analysis of HDPE in Nitrogen (left) and Cronigon S3 (right) atmosphere [24]	46
Fig. 28 Representative DSC heating curve of pure materials, binder system and feedstock for ASA formulations in acetone debindable	47
Fig. 29 Representative DSC cooling curve of pure materials, binder system and feedstock for ASA formulations in acetone debindable	48
Fig. 30 Representative DSC heating curve of pure materials, binder system and feedstock for HDPE-MA formulations in acetone debindable	49
Fig. 31 Representative DSC cooling curve of pure materials, binder system and feedstock for HDPE-MA formulations in acetone debindable	49
Fig. 32 Representative DSC heating curve of pure materials, binder system and feedstock for PP-MA formulations in acetone debindable	51
Fig. 33 Representative DSC cooling curve of pure materials, binder system and feedstock for PP-MA formulations in acetone debindable	51
Fig. 34 Representative DSC heating curve of pure materials, binder system and feedstock for PP-MA formulations in acetone debindable	53
Fig. 35 DSC cooling curve of pure materials, binder system and feedstock for PP formulations in cyclohexane debindable	53
Fig. 36 Representative DSC heating curve of pure materials, binder system and feedstock for HDPE formulations in cyclohexane debindable	54
Fig. 37 Representative DSC cooling curve of pure materials, binder system and feedstock for HDPE formulations in cyclohexane debindable	54
Fig. 38 Representative DSC heating curve of pure materials, binder system and feedstock for PLA formulations in cyclohexane debindable	56
Fig. 39 Representative DSC cooling curve of pure materials, binder system and feedstock for PLA formulations in cyclohexane debindable	56
Fig. 40 Influence of temperature on layer bonding on the examples of PP(H) (top) and of ASA (bottom)	59
Fig. 41 Debonding due to strong material build-up around the steel nozzle on the example of HDPE(H)	59
Fig. 42 Material build-up in the extruder between the gear (left) and gear marks on the filament (right)	60
Fig. 43 Comparison of different printheads, LGX with heatbreak (left), right LGX Shortcut Mosquito Printhead [4]	60
Fig. 44 Debinding results ASA with different backbones	62

Fig. 45 Optical inspection after debinding of the formulations with different backbones	62
Fig. 46 Debinding results of HDPE(AC), PP(AC) and ASA(AC) in acetone after 24h	63
Fig. 47 Debinding results of HDPE(H), PP(H) and PLA(H) in Cyclohexane after 24h	64
Fig. 48 Water debindable test of PVA (left) and PVA/ASA feedstock	65
Fig. 49 Comparison of the average contact angle in water for the binder system and feedstock in cyclohexane debindable (left) and in acetone debindable (right)	67
Fig. 50 SEM images in 2k or 5k magnification of the optimized formulations.	69

9 List of tables

Table 1 Overview of chosen binder systems	8
Table 2 Overview Formulation Composition and Sample names	21
Table 3 Overview of material properties	23
Table 4 Comparison of compounding programs with and without PLA in the formulation	24
Table 5 DSC program overview	26
Table 6 Process parameter compression molding contact angle discs	27
Table 7 Overview of degradation temperatures of the pure materials	40
Table 8 Overview of degradation properties of the PP(AC) and HDPE(AC) feedstock	41
Table 9 Overview of degradation properties of the ASA(AC) feedstock	42
Table 10 Overview of degradation properties of the PLA(H) feedstock	44
Table 11 Overview of degradation properties of the HDPE(H) feedstock	45
Table 12 Overview of degradation properties of the PP(H) feedstock	45
Table 13 DSC Results of pure processed materials, binder system and feedstock for ASA formulations in acetone debindable	48
Table 14 DSC Results of pure processed materials, binder system and feedstock for HDPE formulations in acetone debindable	50
Table 15 DSC Results of pure processed materials, binder system and feedstock for PP formulations in acetone debindable	52
Table 16 DSC Results of pure processed materials, binder system and feedstock for PP formulations in cyclohexane debindable	52
Table 17 DSC Results of pure processed materials, binder system and feedstock for HDPE formulations in cyclohexane debindable	55
Table 18 DSC Results of pure processed materials, binder system and feedstock for PLA formulations in acetone debindable	55
Table 19 Overview on the tested printing parameter finding	58
Table 20 Optimized formulations with printing parameters	61
Table 21 Overview result of contact angle and surface energy for the binder	66
Table 22 Overview KI based programs used in this Master thesis	80

10 Abbreviations and Symbols

Abbreviations	Meaning	Unit
ALF ³	Project Name	-
AISI1	99vol.%Aluminum and 1vol.% Silicium	-
AM	Additive Manufacturing	-
AMF	Additive Manufacturing File	-
ASA	Acrylonitrile Styrene Acrylate	-
BJT	Binder Jetting	-
d90	90% of the particles are below a specific value	µm
DED	Direct Energy Deposition	-
DSC	Dynamic Scanning Calorimetry	
FDM™	Fused Deposition Modelling	-
HDPE	High Density Polyethylene	-
m	Mass	kg
MA	Malein Anhydride	-
MEX	Material Extrusion	-
MIM	Metal Injection Molding	-
MJT	Material Jetting	-
PIM	Powder Injection Molding	-
PLA	Poly lactide	-
PLY	Polygon File Format	-
PP	Polypropylene	-
PTFE	Polytetrafluorethylene	-
PVA	Polyvinyl acetate	-
SLM™	Selective Laser Melting	-
SDS	Shaping Debinding Sintering	-
TGA	Thermogravimetric Analysis	-
TPC	Thermoplastic Copolyester Elastomer	-
TPE	Thermoplastic Elastomer	-
TSEB	Ethylene Butyl Acrylate Copolymer	-
UV	Ultraviolet	-
Vol.%	Volume Percentage	%
VRMF	Virtual Reality Modeling Language	-

Wt. %	Weight Percentage	%
σ_s^d	Surface Tension - Solid Dispersive Part	mN/m
$\dot{\gamma}_{ap}$	Apparent Shear Rate	1/s
R	Nozzle Radius	mm
θ	Contact Angle	°
σ_l^d	Surface Tension - Liquid Dispersive Part	
L	Length of Nozzle	mm
σ_1	Surface Tension - Liquid	mN/m
σ_s^p	Surface Tension - Solid Polar Part	mN/m
η_{ap}	Apparent Viscosity	Pa·s
ϕ	Volume Content	%
V	Volume Flow Rate	m ³ /s
σ_l^p	Surface Tension - Liquid Polar Part	mN/m
σ_s	Surface Tension - Solid	mN/m
γ_{sl}	Interfacial Tension between liquid and solid phase	mN/m
τ_{ap}	Apparent Shear Stress	MPa
η	Dynamic Viscosity	Pa·s

11 Appendix

Table 22 Overview KI based programs used in this Master thesis

Object	Percentage of KI in %	Tool/Version	Comment	Link to prompting
To improve linguistic readability of the text	25 %	Grammarly	n/a	-
To translate	5 %	DeepL	n/a	-